THESIS FOR THE DEGREE OF LICENTIATE OF ENGINEERING

Laser Based Powder Bed Fusion of Plain Carbon and Low-Alloy Steels: Microstructure and Processability

WILLIAM HEARN

Department of Industrial and Materials Science

CHALMERS UNIVERSITY OF TECHNOLOGY

Gothenburg, Sweden 2021

Laser Based Powder Bed Fusion of Plain Carbon and Low-Alloy Steels: Microstructure and Processability
WILLIAM HEARN

Technical report no IMS-2021-1

Department of Industrial and Materials Science
Chalmers University of Technology
SE-412 96 Gothenburg
Sweden
Telephone + 46 (0)31-772 1000

Chalmers digitaltryck
Gothenburg, Sweden 2021

Laser Based Powder Bed Fusion of Plain Carbon and Low-Alloy Steels: Microstructure and Processability

WILLIAM HEARN
Department of Industrial and Materials Science
Chalmers University of Technology

Abstract:
Despite the prominence of laser based powder bed fusion (LB-PBF) as an additive manufacturing technique, the number of alloys that have been approved for the process remains limited. In traditional manufacturing, ferrous alloys are the most common alloy group, consisting primarily of plain carbon and low-alloy steels. However, in LB-PBF, the production of ferrous alloys is limited to a small number of austenitic/precipitation-hardened stainless steels and tool steels. The lack of plain carbon and low-alloy steels stems from the negative impacts of carbon during processing, which promotes the formation of cracking defects within the as-built material. Hence, to expand the opportunities of LB-PBF, an understanding of how to process these carbon-containing ferrous alloys must be established.

This work addresses the LB-PBF processability and microstructure of various plain carbon (0.06 to 1.1 wt.% C) and low-alloy steels (4130, 4140, 4340 and 8620). Microstructural analysis found the as-built specimens to consist of tempered martensite that formed due to the initial rapid cooling and subsequent intrinsic heat treatment that takes place during LB-PBF. Additionally, the presence of retained austenite was observed in alloys with ≥0.75 wt.% C and was caused by the depression of the martensite transformation temperatures, which left some austenite untransformed when cooling to room temperature.

In terms of defects, porosity within the as-built specimens could be related to the chosen volumetric energy density (VED) and the carbon content of the alloy. At low VEDs, specimens contained large, irregular pores that related to lack of fusion porosity, while at high VEDs, specimens contained rounded, medium-sized pores that related to keyhole porosity. In terms of carbon content, increasing the amount of carbon was found to reduce the amount lack of fusion porosity at low VEDs while increasing the amount of keyhole porosity at higher VEDs. The decrease in lack of fusion porosity was caused by the improved wettability and flowability of the melt pool, while the increase in keyhole porosity was caused by increase in melt pool depth with higher carbon contents.

Besides porosity, cold cracking was observed in some plain carbon and low-alloy steels, forming in specimens with a hardness above certain thresholds: ≥425 HV for Fe-C alloys, >460 HV for 4140 alloys and >500 HV for 4340 alloys. Increasing the VED or the laser power decreased the specimen hardness as both factors enhanced the intrinsic heat treatment of LB-PBF. This meant that cracking (in some alloys) could be avoided if a large enough VED or laser power was used. The carbon content also affected the as-built specimen hardness and thus the cracking susceptibility, a finding that explains why low carbon alloys (<0.43 wt.% C) did not display cracking at any of the tested VEDs, whereas high carbon alloys (≥0.75 wt.% C) displayed cracking at every tested VED. Using these findings, processing windows were established that produced high-density (>99.8%), defect-free plain carbon and low-alloy steel specimens without the requirement of build plate preheating.

Keywords: Additive Manufacturing, Laser Based Powder Bed Fusion, Plain Carbon Steel, Low-Alloy Steel, Lack of Fusion Porosity, Keyhole Porosity, Cold Cracking, Intrinsic Heat Treatment

Preface

The work presented in this licentiate thesis was conducted at the Department of Industrial and Materials Science at Chalmers University of Technology between May 2018 and January 2021. The work was conducted within the framework of the Center for Additive Manufacturing – Metal (CAM^2), supported by Vinnova. Research has been carried out under the supervision of Professor Eduard Hryha and Professor Lars Nyborg.

List of Appended Papers:

Paper I: **Processability & Microstructure of Fe-C System via L-PBF**

W. Hearn, E. Hryha, S. Bengtsson, L. Nyborg

Proceedings of EuroPM2019 Conference, 2019

Paper II: **Laser Based Powder Bed Fusion of Fe-C Alloys: Influence of Carbon Content on Microstructure and Processability**

W. Hearn, E. Hryha

Manuscript to be submitted

Paper III: **Microstructural Defects in Low-Alloy Steels Produced by Laser Based Powder Bed Fusion**

W. Hearn, R. Steinlechner, E. Hryha

Manuscript to be submitted

Contribution to Appended Papers:

Paper I: The author planned and executed the majority of the experimental work and analysis of the results. The author wrote the paper in collaboration with the co-authors.

Paper II: The author planned and executed the majority of the experimental work and analysis of the results. The author wrote the paper in collaboration with the co-authors.

Paper III: The author planned and was involved in the execution of the experimental work and analysis of the results with the co-authors. The author wrote the paper in collaboration with the co-authors.

TABLE OF CONTENTS

CHAPTER 1 – INTRODUCTION

Additive manufacturing (AM) offers a design freedom that is not available in traditional manufacturing. This freedom, combined with the ability to consolidate parts, produce components with high material/functional complexity and reduce lead time, has created a use-case for AM in the aerospace, automotive, tooling and medical industries [1]. Growth has been particularly significant for metal-based AM: Over the past decade, annual growth rates have exceeded 20%, and the metal AM industry was expected to reach a value of $20 billion by 2020 [2].

One of the most prominent metal AM techniques is laser based powder bed fusion (LB-PBF), which uses thermal energy from a focused laser source to selectively fuse regions of a powder bed. Yet, even with the noticeable growth of metal AM, LB-PBF remains limited to a select group of alloy systems, namely aluminum alloys, titanium alloys, nickel based alloys, stainless steels, tool steels and precious metals [1]. In traditional manufacturing, ferrous alloys are by far the most commonly used set of metallic materials, where more than 90% of said alloys are classified as either plain carbon or low-alloy steels [3]. Comparatively, in LB-PBF, ferrous alloys are limited to austenitic stainless steels, precipitation-hardened stainless steels or tool steels. This lack of plain carbon and low-alloy steels severely hinders the application of LB-PBF components and represents a large gap within the technology.

One of the main reasons why plain carbon and low-alloy steels are not commonly used relates to the challenges brought on by carbon during processing, as this carbon can induce cracking within the material [4] [5]. Due to the rapid solidification that takes place during LB-PBF, carbon will promote the formation of the hard and brittle martensite phase. This result, combined with the residual stresses that form due to rapid solidification [6] and due to the formation of martensite [4] [7], can lead to cracking and delamination of the material. Such cracking must be avoided as internal defects, especially those close to the surface [8] [9] and those with an elongated shape [10] [11], can severely reduce the mechanical property performance of AM components. The current understanding of how to successfully process carbon-containing ferrous alloys comes from the analysis of tool steels, where it was found that the application of build plate preheating can limit this cracking issue [4] [12] [13].

Despite this knowledge base, limited data is available regarding the processing of carbon-containing ferrous alloys in literature, especially when working with plain carbon and low-alloy steels. Additionally, there is a general lack of knowledge regarding how changes in the carbon content will affect the processability, crack susceptibility and microstructure of ferrous alloys. Hence, to expand the use of LB-PBF, the processability of plain carbon and low-alloy steels must be better understood.

1.1 RESEARCH OBJECTIVES

The objective of this research is to provide a basic understanding of the processability and microstructure of LB-PBF-produced plain carbon and low-alloy steels when no build plate preheating is applied. Understanding the effect of both the carbon content and the processing conditions will allow for the establishment of robust processing windows that produce high-density, defect-free components. These objectives are summarized in the following research questions:

RQ1: How does the carbon content affect the microstructure and defect formation of LB-PBF-produced plain carbon and low-alloy steels?
RQ2: How can the processing conditions affect defect formation?
RQ3: What are the limits of carbon content for LB-PBF fabrication of high-density, defect-free specimens without the use of build plate preheating?

CHAPTER 2 – BACKGROUND

2.1 PLAIN CARBON AND LOW-ALLOY STEELS

Plain carbon and low-alloy steels represent one of the most prominent alloy groups and are used in applications where hardness, strength, ductility, toughness and wear resistance are required while still maintaining a low materials cost. The hardness and mechanical properties are primarily derived from the carbon content, as this will dictate the alloy hardenability [14]. Plain carbon and low-alloy steels are typically used in structural components, ranging from bolts and studs to more advanced applications such as pressure vessels [15] [16].

Plain Carbon Steels

Plain carbon steels refer to ferrous alloys with less than ~2 wt.% of alloying elements, where the Mn, Si, Cu, P and S content cannot exceed 1.65 wt.%, 0.6 wt.%, 0.6 wt.%, 0.04 wt.% and 0.06 wt.%, respectively [15]. This alloy group can be further subdivided based upon the carbon content. Low-carbon steels contain up to 0.3 wt.% C and are commonly used in applications where high formability is required (e.g. automotive body panels and wire products) [17]. Medium-carbon steels contain 0.3 to 0.6 wt.% C and are used when better mechanical properties are required (e.g. gears, bolts, hand tools and wear resistant parts) [17]. High-carbon steels contain 0.6 to 1.0 wt.% C and are used as edge tools or in wear-resistant parts [15]. However, these alloys are limited in their application as their high hardenability reduces their formability and weldability. Finally, there are ultra-high-carbon steels (1.25 to 2 wt.% C), which are used in similar applications as high-carbon steels.

Low-Alloy Steels

Low-alloy steels refer to ferrous alloys with less than ~10 wt.% of alloying elements, where the Mn, Si and Cu contents cannot exceed 1.65 wt.%, 0.6 wt.% and 0.6 wt.%, respectively [15]. These alloys can be further subdivided based upon their carbon content, either as low-carbon (<0.3 wt.% C) or medium-carbon (0.3 to 0.6 wt.% C) grades. Low-alloy steels exhibit superior mechanical properties in comparison to plain carbon steels as the increased amount of alloying additions improves alloy hardenability. Such alloying additions also affect the transformation and stability of phases within the material. In low-alloy steels, alloying elements are categorized as either austenite or ferrite stabilizers, where austenite stabilizers refer to elements that widen the temperature stability of austenite (e.g. C, Ni, Co and Mn), while ferrite stabilizers refer to elements that narrow the temperature stability of austenite and instead promote the formation of ferrite (e.g. Cr, Si, S, P and Mo).

Although a wide range of low-alloy steels exists, the current study focused on Cr-Mo (4130 and 4140) and Ni-Cr-Mo (4340 and 8620) low-alloy steels. The typical alloying elements in these alloys are Ni, Cr, Mo, Mn and Si, and the general effects of each alloying element can be summarized as follows [15] [16]:

- ***Nickel:*** Added to act as an austenite stabilizer and to improve corrosion resistance.
- ***Chromium:*** Added to improve alloy hardenability, to promote carbide formation and to improve corrosion/oxidation resistance.
- ***Molybdenum:*** Added to improve alloy hardenability and to promote carbide formation.
- ***Manganese:*** Added to increase alloy hardenability at moderate cost, to form non-harmful sulfides and to promote carbide formation.
- ***Silicon:*** Added to help with deoxidation and to improve material strength in the quenched and tempered condition.

2.2 ADDITIVE MANUFACTURING

Additive manufacturing (AM) represents a group of processing techniques that utilize a layer-by-layer approach to produce components directly from computer-aided designs (CAD). At the beginning of the AM process, a CAD file provides a digital, 3D representation of the component. Next, this file is converted into an STL format that will segment the original 3D file into a collection of 2D representations. Once converted, this STL file is sent to the AM machine for printing. After printing, the component is removed and undergoes the required post-processing steps so it can be used in its intended application. To date, the major AM processes can be separated into seven main categories according to the ASTM-52900 standard [18]:

1. VAT photopolymerization
2. Powder bed fusion
3. Material extrusion
4. Material jetting
5. Binder jetting
6. Directed energy deposition
7. Sheet lamination

The focus of this study was on the production of plain carbon and low-alloy steels when using the AM technology of laser based powder bed fusion (LB-PBF).

2.3 LASER BASED POWDER BED FUSION (LB-PBF)

2.3.1 Background

LB-PBF is an AM technique that uses thermal energy, provided by a focused laser source, to selectively fuse regions of a powder bed layer-by-layer to produce 3D components. The ability to make these components directly from CAD files allows for a design freedom that cannot be achieved when using conventional processes. LB-PBF can also produce functionally graded materials [19] and can produce components on demand, reducing lead time and the need for maintaining large component inventories. These capabilities have made LB-PBF an attractive manufacturing technique within the aerospace, medical, tooling and automotive sectors [1].

Despite these advantages, there are limitations associated with the technology. First, the process has low build rates and small build volumes. These factors lead to long processing times and a limitation in the size/number of components that can be produced during a single process run. LB-PBF also requires noticeable post-processing to: (i) remove support structures (ii), heat treat the material to achieve the required microstructure and to remove residual stresses and (iii) improve the surface roughness to improve the mechanical property performance. All these post-processing steps increase not only the final production time but also the final production cost. The last and arguably most important limitation of LB-PBF is the limited number of materials that have been approved for the process. Currently, fewer than 40 metal alloys are commercially available for LB-PBF, which is significant fewer than those available in other powder-based production techniques.

Considering these factors, the current use-case for LB-PBF is the production of small, complex components of which relatively small quantities are required (Figure 1a). This is because unlike traditional processes, LB-PBF can add both individualization and complexity “for free” depending upon the lot size and the part complexity (Figure 1b-c).

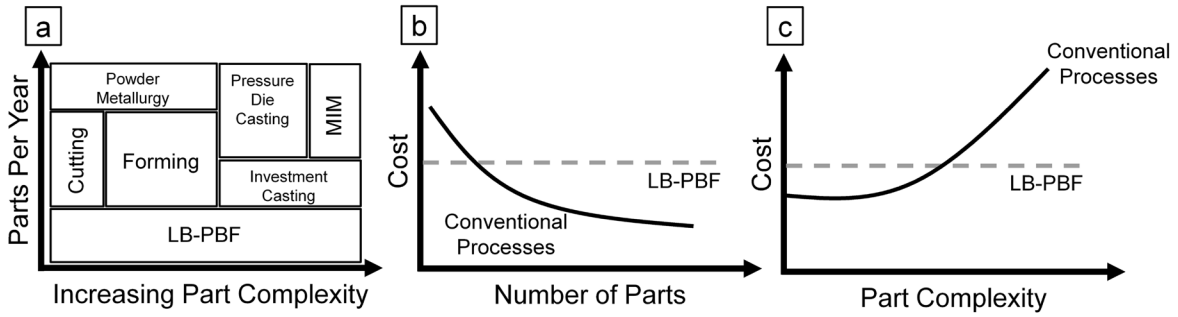

Figure 1: (a) Comparison of laser based powder bed fusion (LB-PBF) to conventional techniques with respect to parts per year and part complexity. (b) Comparison of LB-PBF to conventional processes with respect to cost and number of parts. (c) Comparison of LB-PBF to conventional processes with respect to cost and part complexity. Adapted from [20].

2.3.2 Working Principle

A typical LB-PBF machine is composed of a powder reservoir, a recoating mechanism, a building platform, a collector bin and a laser source that are all enclosed within a building chamber (Figure 2). The LB-PBF build cycle begins when a thin layer of metal powder (supplied by the reservoir) is spread across the building platform by the recoating mechanism. After the spreading of this powder layer, the laser source selectively exposes regions of the powder bed. Following this selective exposure, the build platform is lowered, the recoating mechanism moves back to its original position and the described process repeats itself until all layers of the component have been printed. This processing occurs in an inert environment that is maintained via a constant flow of inert gas within the building chamber.

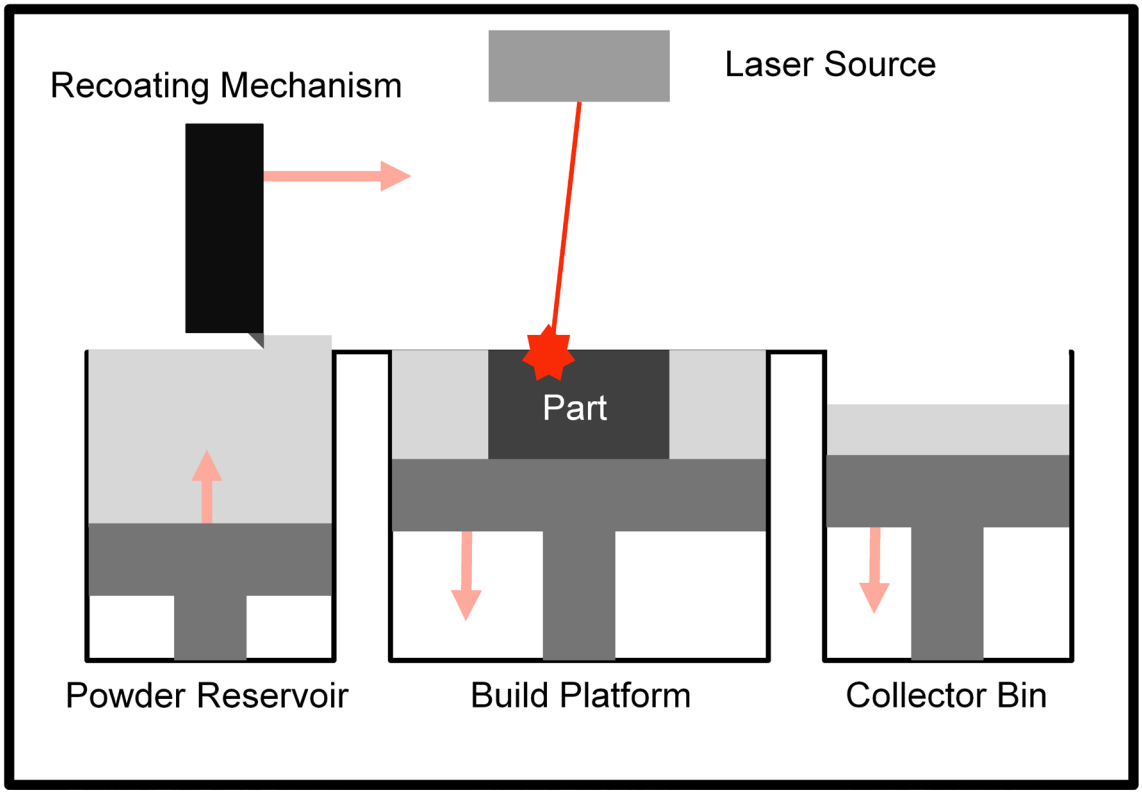

Figure 2: Schematic of the typical components of an LB-PBF machine. The powder is depicted as the light grey regions, while the arrows indicate the typical motion of the specified components during the build cycle.

2.3.3 Feedstock Material

In LB-PBF, metal powder (with a size range of 10 to 60 µm) is used as the feedstock material. This metal powder is typically manufactured using gas atomization as this technique can produce spherical powders with high packing density and a controlled particle size distribution while maintaining lower costs and high powder yields [20]. Examples of gas atomized powder are shown in Figure 3.

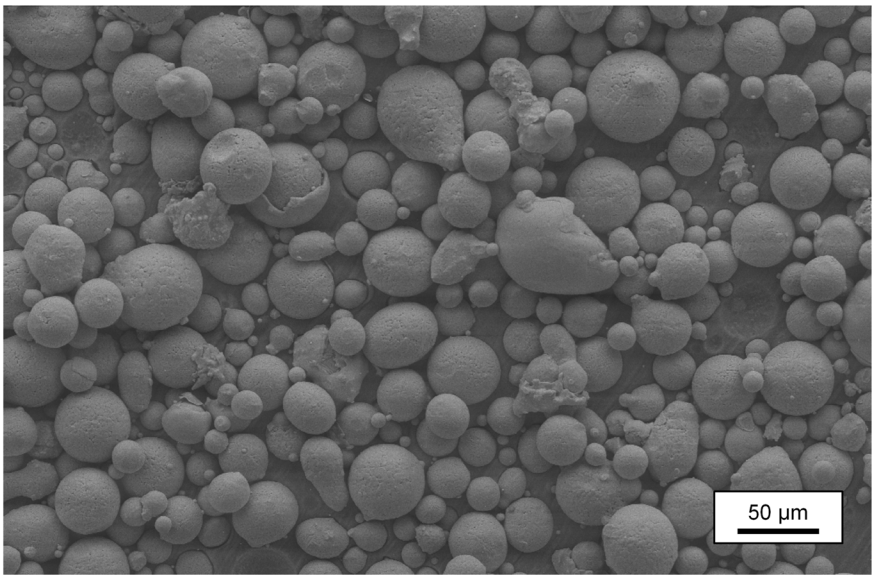

Figure 3: Example of gas-atomized Fe-1.1C alloy powder.

Gas atomization uses the pressurized flow of inert gas to facilitate the atomization process (Figure 4). At the beginning of inert gas atomization, molten material within a tundish flows into the atomization chamber. This molten material is subsequently atomized by the flow of inert gas (Ar or N_2), which facilitates the breakup of the material into many small droplets. As these droplets fall, they solidify and are collected at the bottom of the atomization chamber.

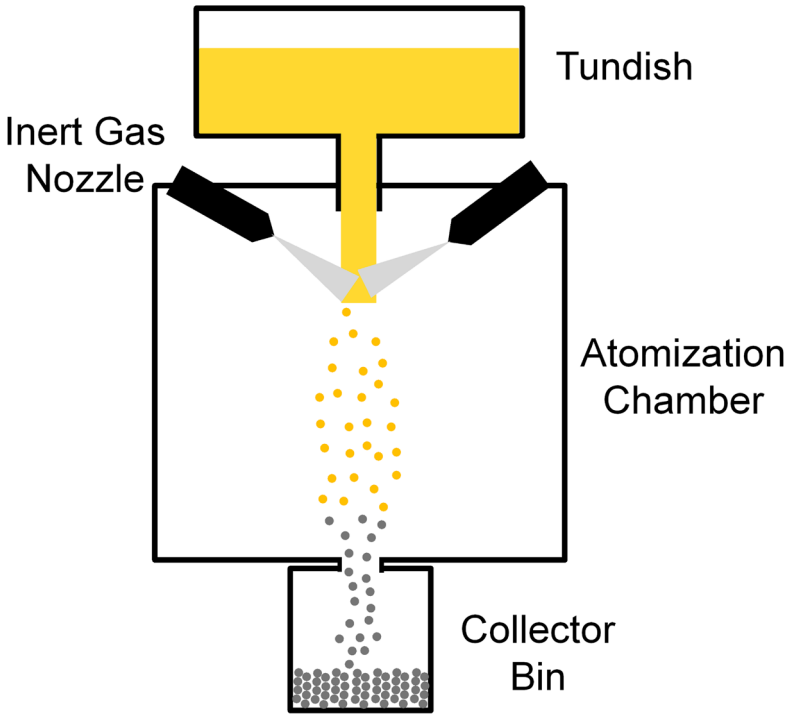

Figure 4: Schematic of the gas atomization process. Adapted from [20].

The quality of LB-PBF components can be affected by the characteristics of the powder feedstock, specifically the chemical composition, particle size distribution, powder morphology and rheological properties [20]. The importance of these characteristics is primarily related to their effect on powder flowability and powder packing density, as these factors can affect defect formation during LB-PBF [21] [22]. Having relatively spherical powders with a controlled particle size distribution is important as this can improve powder flowability and packing [23] [24]. The characteristics of the powder feedstock are dependent on the chosen manufacturing process [25] as well as the number of times the powder has been recycled [21] [26] and how this powder recycling was conducted [27]. However, a clear correlation between powder properties and component performance has yet to be firmly established and is the subject of ongoing research [27].

2.3.4 Processing Parameters

In LB-PBF, the important processing parameters can be broken into three main groups: (i) process-related parameters, (ii) laser-related parameters and (iii) scan-related parameters.

Process-Related Parameters

Process-related parameters refer to a variety of aspects such as the recoater speed, powder layer thickness, processing atmosphere, and build plate preheating. The speed of the recoater is important as it influences the surface uniformity and packing of the powder bed [28]. While increasing the layer thickness can increase the build rate, it can also increase the surface roughness [29] and lead to the formation of large defects within the as-built material [29] [30]. With respect to the processing atmosphere, many aspects must be considered. The first is control of the oxygen content as this can induce defect formation [31]. Additionally, the flow of inert gas must be large enough to remove unwanted process by-products from the laser exposure area [32] Lastly, the chosen inert gas (Ar, N_2 or He) will affect the rate of heat extraction and subsequently the as-built microstructure [33]. As for build plate preheating, this is typically used to reduce the residual stress within the as-built material [4] [34] as preheating can lower both the thermal gradient and the cooling rate [35].

Laser-Related Parameters

Laser-related parameters refer to characteristics such as the laser source, wavelength, power and beam diameter. Most LB-PBF machines are equipped with Yb-fiber lasers as their shorter wavelength promotes improved absorptivity in metal powders (when compared to CO_2 lasers) [36]. In addition, Yb-fiber lasers provide improved efficiency and stability and entail lower maintenance costs (when compared to Nd:YAG lasers) [37]. The ability of the heat source to fully melt the material is paramount during LB-PBF and is primarily controlled by the power density distribution, which is a function of the total power (P), heat source radius (r_b), radial distance from the heat source axis (r) and distribution factor (f) [35]:

$$P_d = \frac{fP}{\pi r_b^2} \exp\left(-f\frac{r^2}{r_b^2}\right) \tag{2.1}$$

To date, most work with laser based parameters has focused on the laser power and the laser beam diameter, as both are key components of the power density distribution and will affect melt pool formation during LB-PBF [38] [39] [40] [41] [42]. In LB-PBF most lasers utilize a Gaussian power density distribution [43]. This type of distribution has the greatest laser intensity and inputted energy at the center of the laser beam, with the intensity decreasing as the radial distance from the center increases (Figure 5).

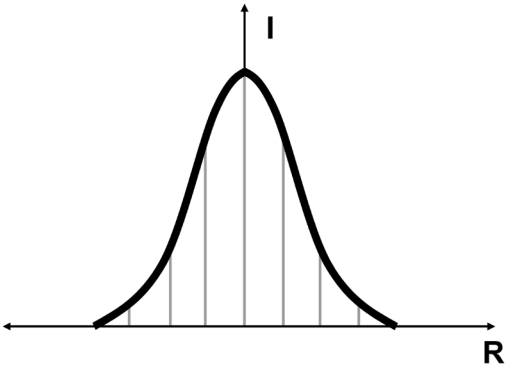

Figure 5: Schematic outlining a Gaussian power density distribution. The area under the curve represents the inputted laser power at a specific distance from the center of the laser beam. Adapted from [43].

Scan-Related Parameters

Scan-related parameters control how the laser scans across the powder bed and include characteristics such as the scanning speed, the spacing between scan tracks and the scanning strategy. Maintaining a proper scan speed is important as this will influence the size and stability of the melt pool [40] [44] [45] [46], while the scan spacing must be controlled to ensure adequate overlap between deposited melt tracks [47] [48]. The other important scan-related parameter is the scanning strategy, which refers to the specific path of the laser as it moves across the area of exposure. The first aspect of the scanning strategy relates to the various regions of exposure (Figure 6). The core exposure relates to the exposure of the bulk area, while the contour exposure relates to the exposure along the edges. This contour exposure is beneficial as it can improve surface roughness [49] and can be utilized to remove porosity that forms when the laser turns around at the end of a scan track [50].

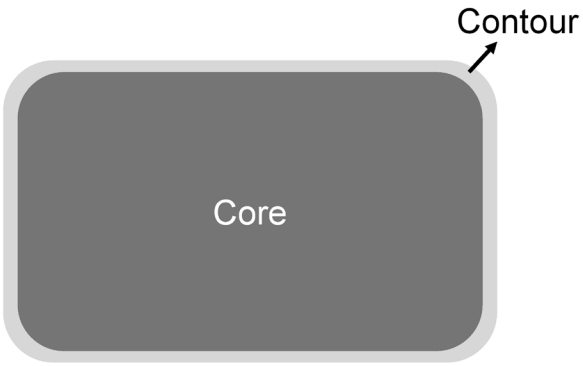

Figure 6: Schematic outlining the regions of core exposure (dark grey) and contour exposure (light grey).

During core exposure, different paths of the laser can be applied. The most basic is unidirectional scanning, in which the laser vectors all travel in the same direction (Figure 7a). The other basic scan pattern is bi-directional scanning, in which the direction of the laser vectors alternates (Figure 7b). More complicated core exposure strategies have also been developed. One is the island scan strategy, which divides the area of exposure into several regions that are individually exposed (Figure 7c). Another is the stripe scan strategy, which is the most commonly used exposure pattern and divides the area of exposure into several stripes (that are individually exposed), where the translational direction of the laser is alternated by 180° after each stripe (Figure 7d). The last component of the scanning strategy is the angle of rotation between layers. Typically, LB-PBF uses a rotation angle of 67° as this orientation provides the maximum number of orientations before the original orientation is repeated [51].

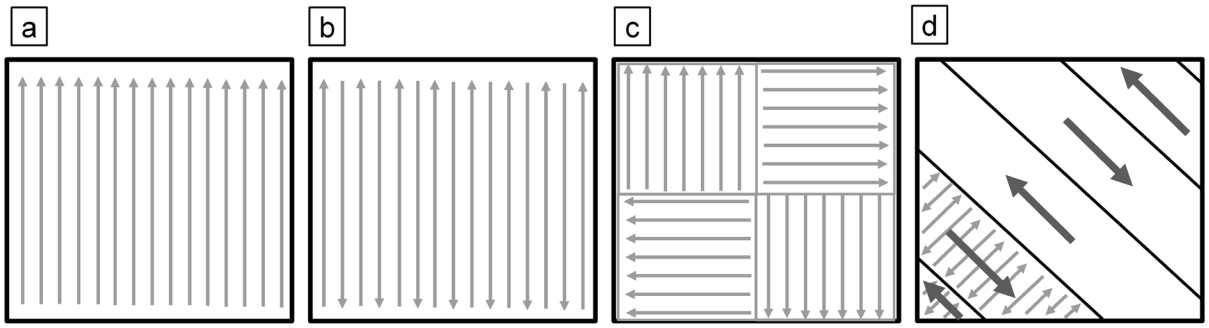

Figure 7: (a) Unidirectional scanning pattern, (b) bi-directional scanning pattern, (c) island scanning pattern, (d) stripe scanning pattern where the dark grey arrows represent the translational direction of the laser.

Volumetric Energy Density

In LB-PBF the main goal is to produce a fully dense material. To achieve this goal, an adequate energy input is required that induces full melting of the material while also ensuring adequate overlap between deposited melt tracks and between deposited layers. A combined processing parameter that describes these requirements is the volumetric energy density (VED); see Figure 8.

$$VED = \frac{P}{v*h*l} \tag{2.2}$$

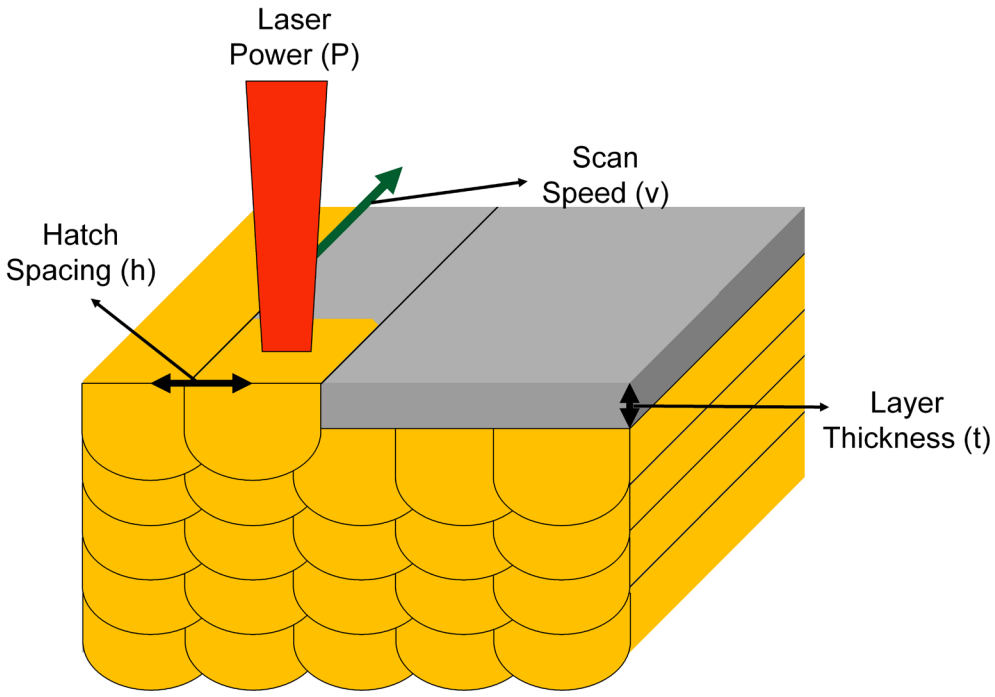

Figure 8: Schematic outlining the parameters of volumetric energy density (VED), which provides a representation of the total inputted energy as a function of the laser power (P), scan speed (v), hatch spacing (h) and layer thickness (t).

There are limitations with the VED as it is only describes the inputted energy from the laser source and does not provide information regarding the complex heat and mass transport that occurs within the melt pool. At the same time, the parameters of the VED have been shown to affect the melt pool size and morphology [40] [44] [45] [46]. This means that while VED is not a magic number that describes all aspects of LB-PBF, it still represents a combination of important processing parameters that can be used to outline specific processing windows.

2.3.5 Melt Pool Formation and Dynamics

During LB-PBF the formation of the melt pool is dependent upon the interaction of the laser source and the powder feedstock. When the laser beam first contacts a powder particle, some of the inputted energy is absorbed, while the rest is reflected away. This reflected energy then contacts another powder particle, and the process repeats itself until the intensity of the reflected energy becomes negligible or the laser beam is reflected outside of the powder bed [52]. Due to the rapid scan speeds that are used during LB-PBF, the irradiation of the powder occurs over very short time scales of around 0.2 to 8 ms [53]. Hence, the melting of a powder particle also occurs rapidly (~2 µs for Ti powder [54]) due to the high-power density of the laser source. As several powder particles melt and coalesce, a melt pool is formed.

The morphology of the melt pool is first dependent upon the mode of heat transfer between the laser and the powder bed. Typically, in other laser based production techniques (e.g. welding), the heat transfer is considered to be either in conduction mode or in keyhole mode [55]. During conduction mode, heat is transferred to the material via conduction from the heated surface, forming a wide but shallow melt pool. Conversely, during keyhole mode, a deep, keyhole-shaped depression forms due to material evaporation. This causes heat transfer to occur not only via conduction from the heated surface but also via conduction from the interior of the keyhole depression [56], thus leading to a deeper and narrower melt pool when compared to conduction mode melting. Typically, the transition between the two modes occurs when the power density is high enough to initiate material evaporation [38].

The peak temperatures during LB-PBF can reach as high as the vaporization temperature [57] [58]. When these temperatures are reached, a metallic vapor jet forms, creating a high recoil pressure that exerts a downward force on the melt pool and causes a keyhole-shaped depression to form [57]. Past studies [40] [58] have found that this depression is a common characteristic of the melt pool during LB-PBF, in the range of relevant processing parameters, pointing to some amount of vaporization taking place. This recoil pressure can also lead to the ejection of powder particles when it exceeds the surface tension forces within the melt pool [59]. Ejection of powder particles is also influenced by the ambient gas flow within the processing chamber, where said flow will accelerate entrained particles towards the vapor jet, causing them to be (i) pulled into the melt pool, (ii) ejected out as a cold particle or (iii) pulled into the laser beam and ejected out as hot spatter [57] (Figure 9).

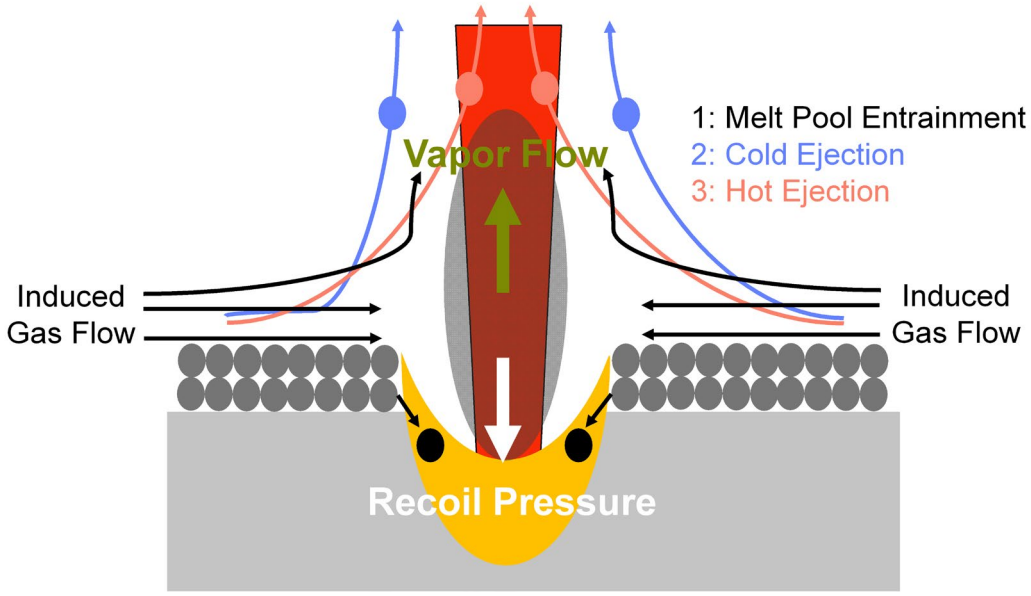

Figure 9: Schematic outlining the formation of a melt pool depression due to recoil pressure. Additionally, the various types and paths of entrained particles during LB-PBF are highlighted. Adapted from [57].

Upon cooling below the vaporization temperature, surface tension begins to dominate the movement of molten material within the melt pool, creating a strong convective flow referred to as Marangoni flow. This Marangoni flow is a result of the non-uniform temperatures within the melt pool, which create surface tension gradients, typically inducing flow from regions with low surface tension to regions with high surface tension. The strength of this convective flow can be estimated using the Marangoni number:

$$M_a = \frac{d\gamma_{LV}}{dT}\frac{dT}{ds}\frac{L}{2\eta\delta} \tag{2.3}$$

Where $\frac{d\gamma_{LV}}{dT}$ is the surface tension gradient, $\frac{dT}{ds}$ is the thermal gradient, L is the characteristic length of the melt pool, η is the viscosity and δ is the thermal diffusivity. The direction of Marangoni flow is dependent upon the sign of the surface tension gradient. Typically, for pure metals and many alloys, a negative surface tension gradient is present [45]. In such a scenario, flow within the melt pool moves away from the center, leading to a wider and shallower melt pool that has a surface profile with more material located at the melt pool edges (Figure 10). However, if an alloy contains the noticeable presence of surface-active elements (e.g. O, S, N) then the surface tension gradient will shift to a positive value [60] [61]. This causes flow towards the melt pool center, promoting a deeper and narrower melt pool that has a surface profile with more material located at the melt pool center (Figure 10).

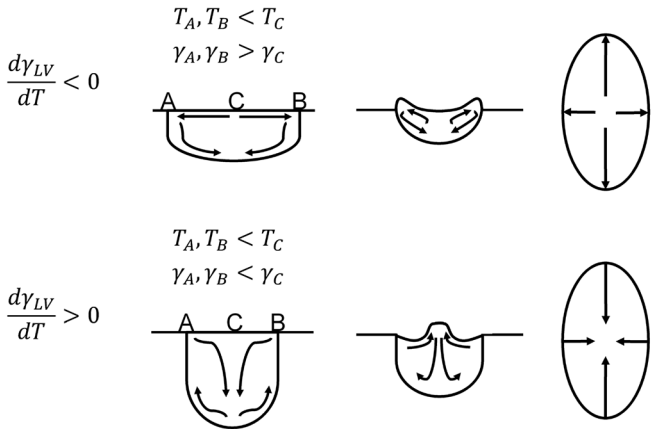

Figure 10: Schematic outlining the direction of Marangoni flow within the melt pool depending upon the sign of the surface tension gradient. Adapted from [61] [62].

2.4 Microstructure of Plain Carbon and Low-Alloy Steels Produced by LB-PBF

As with other processes, the microstructure of plain carbon and low-alloy steels produced by LB-PBF is dependent on the experienced thermal history. In LB-PBF, the thermal history can be divided into two stages: (i) the initial solidification of the material and (ii) the intrinsic heat treatment that occurs during processing (Figure 11).

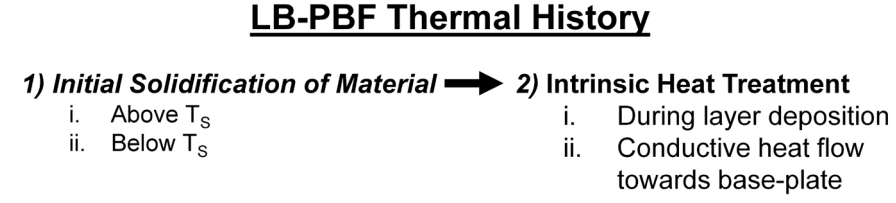

Figure 11: Stages of the thermal history during LB-PBF.

Stage 1: Initial Solidification

The initial solidification of the material can be divided into two parts: (i) cooling to the solidus temperature (T_s) and (ii) cooling below the solidus temperature (T_s). In plain carbon and low-alloy steels, cooling to the T_s is important as this will affect the solidification structure. The growth of this structure is controlled by the temperature gradient (G) and the growth rate (R), where G/R determines the structure morphology, while G*R (e.g. cooling rate) determines the structure fineness [62] (Figure 12). Since cooling rates of up to 10^6 K/s [58] [63] can be achieved during LB-PBF, very fine solidification structures can be obtained. As for the solidification morphology, ferrous alloys produced by LB-PBF typically display a cellular structure [64] [65] due to the large thermal gradients and cooling rates that are present during processing.

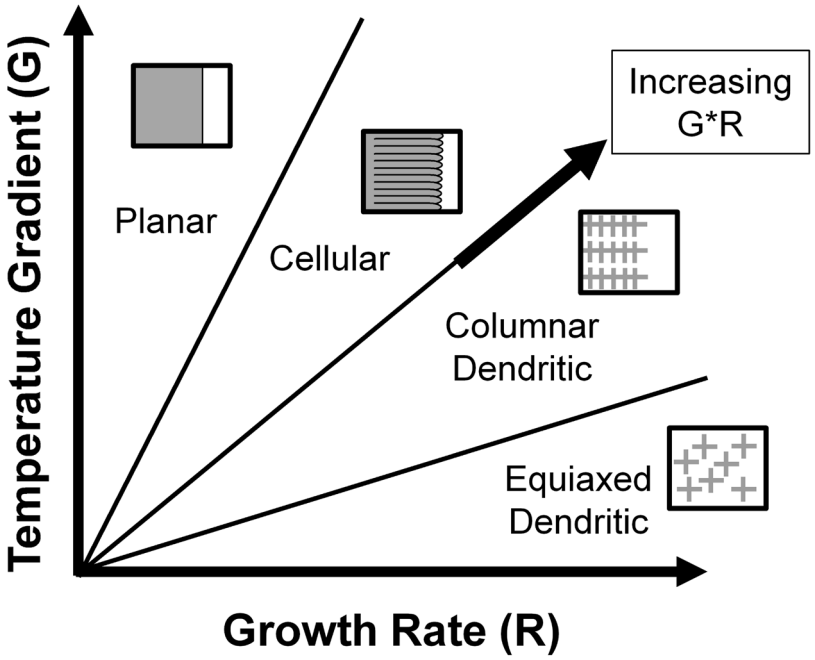

Figure 12: Schematic outlining the influence of growth rate (R) and temperature gradient (G) on the morphology of the formed solidification structure. Adapted from [62].

As for the cooling that occurs below the T_s temperature, this is where the martensite transformation takes place. The formation of martensite is both diffusionless and athermal, occurring when the cooling rate exceeds the diffusion rate of carbon atoms [66]. Under these conditions the carbon atoms have insufficient time to diffuse and form the typically stable cementite (Fe_3C). Instead they become entrapped at octahedral interstitial sites of the face-centered cubic (FCC) austenite lattice, transforming it into the strained body-centered tetragonal (BCT) lattice structure of martensite.

Since the transformation is athermal, the amount of transformed martensite is dependent upon the undercooling of the system. The temperature at which this transformation begins is referred to as the martensite start (M_s) temperature and represents the required thermodynamic driving force to initiate the shear transformation of austenite to martensite [66]. Increasing the carbon content will lower the M_s as a greater amount of carbon will be in solution, increasing the shear resistance of the parent austenite phase. The temperature that marks the full transformation of austenite to martensite is referred to as the martensite finish (M_f) temperature, which is also depressed as the carbon content increases. If the carbon content is high enough, then the full transformation to martensite cannot be achieved at room

temperature, leading to the presence of untransformed austenite [67] [68]. The M_s is also influenced by other alloying elements, the addition of which (except for cobalt and aluminum) will lower the transformation temperature [66] [69]. In addition to alloy composition, a relationship between the parent austenite grain size and the M_s temperature has been reported [70] [71], where a decrease in the parent austenite grain size will depress the M_s temperature due to a non-chemical contribution to the Gibbs energy of the martensite transformation.

The factors that determine the morphology and substructure of the transformed martensite remain poorly defined. However, considerations such as the M_s temperature, the austenite stacking fault energy, the critical resolved shear stress for slip/twinning and the strength of the austenite/martensite phases are important factors to consider [72]. In carbon-containing steels, two major martensite morphologies are present, lath and plate martensite. The ranges at which these morphologies form is dependent on the carbon content (Figure 13). A dominant lath morphology is present at carbon contents of ≤ 0.6 wt.% C, while a dominant plate morphology is present at carbon contents ≥1 wt.% C [72]. In between these compositions, a mixed morphology of lath and plate martensite is expected.

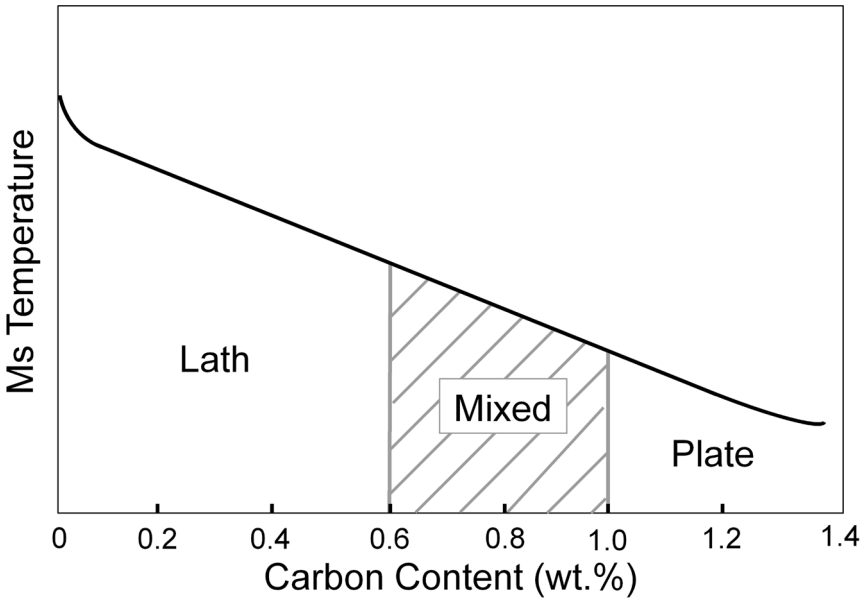

Figure 13: Schematic outlining the evolution of martensite morphology in Fe-C alloys as a function of the carbon content. Adapted from [67].

Stage 2: Intrinsic Heat Treatment

After rapid quenching from the liquid state, the deposited material will undergo an intrinsic heat treatment as new layers are deposited on top of previously solidified layers. When a new layer is deposited during LB-PBF, the powder plus solidified material that is heated above the liquidus temperature (T_L) will form the new melt pool, while the material that is heated above the stability temperature of austenite (A_{e3}) will reform into austenite and subsequently into untempered martensite upon rapid cooling. The rest of the material (that is not re-melted or retransformed) will undergo an intrinsic heat treatment that relates to a cyclic type of re-heating, consisting of many short spikes in temperature [73] [74] [75].

There is also an intrinsic heat treatment that occurs progressively during LB-PBF and is a result of the conductive heat flow that moves in the direction of the build plate. Past studies have demonstrated that the thermal conductivity of the solidified material is approximately 100 times larger than that of the surrounding powder bed [76]. Additionally, the build plate has been shown to act as a heat sink [35].

These factors lead to a consistent, conductive heat flow that is directed towards the build plate through the already solidified material.

Understanding this intrinsic heat treatment is important as it will noticeably alter the martensite that initially formed during the first stage of the thermal history. When first formed, the martensite will be in a non-equilibrium, highly unstable state due to a variety of factors, including the supersaturation of alloying elements, the high density of martensite crystal interfaces, the high dislocation density and the potential presence of retained austenite [72]. Freshly formed martensite is thus highly susceptible to phase transformations during heat treatment. The classic stages of martensite tempering in ferrous alloy can be described as such [72]:

- ***Stage 1 (100–200 °C):*** Involves the precipitation of fine transitional carbides (e.g. Fe_2C).
- ***Stage 2 (200–300 °C):*** Involves the decomposition of untransformed or retained austenite into a mixture of cementite + ferrite.
- ***Stage 3 (< Eutectoid Transformation Temperature [A_{e1}]):*** Involves the replacement of transitional carbides with cementite (Fe_3C).
- ***Stage 4 (< Eutectoid Transformation Temperature [A_{e1}]):*** Relates to the alloy-dependent stage of tempering that can overlap with the tempering that occurs in Stage 3.

Despite this classical understanding of martensite tempering, it is difficult to directly apply it to what happens during LB-PBF because the intrinsic heat treatment is location dependent, takes place over very short time scales and will occur each time a new melt track is deposited. Due to this complexity, the understanding of the as-built microstructure in LB-PBF-produced plain carbon and low-alloy steels is not fully developed and is an area of ongoing research.

2.5 Defects in Plain Carbon and Low-Alloy Steels Produced by LB-PBF

This section outlines the relevant defects that can form in plain carbon and low-alloy steels produced by LB-PBF. Additionally, it discusses why each defect should be limited and what mitigation strategies can be used.

2.5.1 Balling

Balling is a phenomenon in which the deposited melt track does not wet the underlying substrate and instead spherodizes into agglomerates due to surface tension forces [77]. This spherodization creates a beaded melt track that obstructs the deposition of subsequent powder layers and detrimentally affects the as-built specimen density [77] [78]. Past research has found that increasing the VED can reduce balling; as increasing the laser power [77] [78] [79], decreasing the scan speed [78] [79] and decreasing the layer thickness [78] have proven to be effective mitigation strategies. In addition, reducing the oxygen content within the processing atmosphere [78] and within the powder feedstock [80] have also proven effective. However, the current understanding of balling primarily relates to the deposition of a layer onto a substrate made of a different material, leaving a limited understanding of how or when balling occurs during the deposition of subsequent layers during LB-PBF when non-equilibrium wetting conditions are present [81]. Additionally, balling has been found to be more prevalent during the production of single tracks than during the production of multiple layers [45].

2.5.2 Porosity

Lack of Fusion Pores

Lack of fusion porosity relates to irregular pores that form between deposited layers and between deposited melt tracks due to an insufficient energy input (Figure 14). Inter-layer lack of fusion occurs

when the penetration of the melt pool is insufficient to bond with the substrate or with the previously deposited layer, while lack of fusion between melt tracks occurs when the overlap between tracks is insufficient. Lack of fusion can also occur due to ejected particles that subsequently interfere with the interaction between the laser source and the powder bed [82]. Limiting lack of fusion porosity is of high importance as its presence negatively affects both tensile [10] [83] [84] and fatigue properties [11] [85]. This effect is due to the large size and irregular shape of said pores, which causes them to act as stress concentrators where failure or fatigue cracks can initiate.

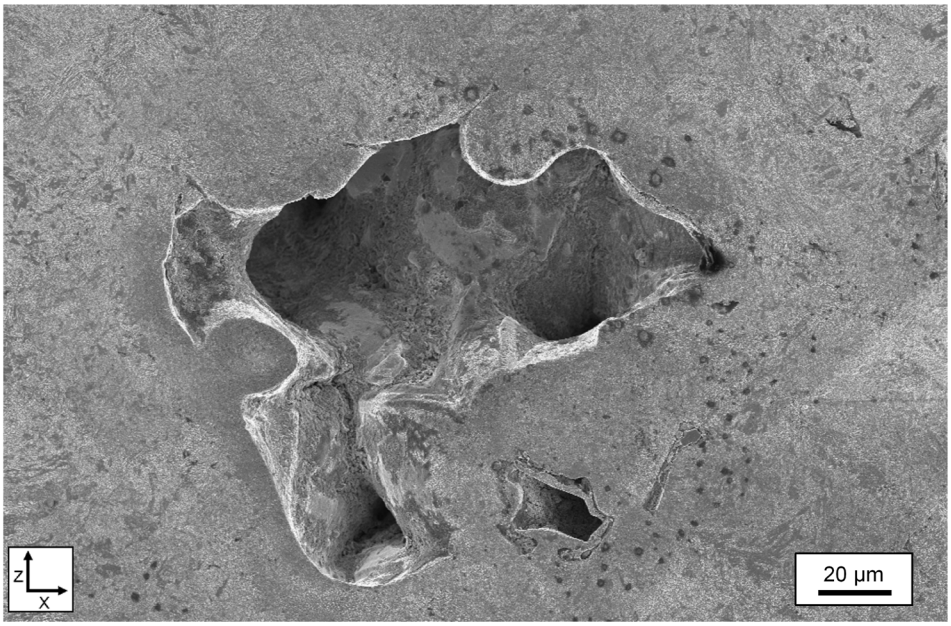

Figure 14: Lack of fusion porosity in Fe-0.2C specimen produced at 60 J/mm^3 using a 110 W laser power.

To limit lack of fusion porosity, the correct processing parameters must be selected. Increasing the laser power and decreasing the scan speed will reduce lack of fusion porosity as both increase the depth and width of the formed melt pool [39] [40] [44], ensuring better overlap between layers and between melt tracks. Reducing the hatch spacing has also been shown to reduce lack of fusion porosity [86] [87], as this lowers the required overlap between melt tracks. Additionally, decreasing the value of the layer thickness has been found to reduce the formation of lack of fusion porosity [29] [30].

Besides the processing parameters, the material properties will also influence the formation of lack of fusion porosity as these properties affect the size and wetting behavior of the melt pool. The melt pool size is influenced by the materials' absorptivity, melting temperature, thermal conductivity, density and heat capacity [47] [48], while the wetting behavior is primarily dependent on the alloys' surface tension and viscosity [76] [81].

Keyhole Pores

Keyhole porosity relates to rounded pores that form due to instabilities of the vapor depression during keyhole mode melting (Figure 15) [88] [89]. Typically, this porosity forms when using high laser powers and low scan speeds, as both factors increase the likelihood and depth of the vapor depression [40]. However, the laser beam diameter and the materials' boiling temperature can also play a role [90]. In comparison to lack of fusion porosity, keyhole pores are not as detrimental to the mechanical properties of the as-built specimens [11] [83]. However, if they have a pronounced presence [83] or are located close to the specimen surface [8] [91], they can still lead to a reduction in mechanical property performance, especially fatigue strength.

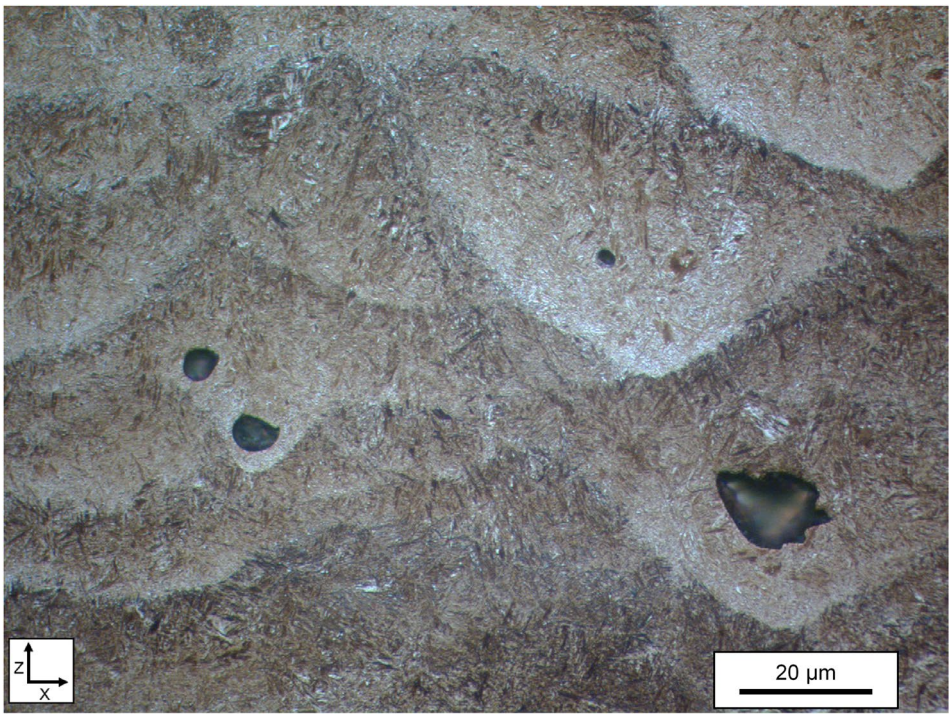

Figure 15: Keyhole pores in an Fe-0.75C alloy specimen produced at 160 J/mm^3 using a 110 W laser power.

The mechanisms behind the formation and entrapment of keyhole porosity during LB-PBF are still being developed. Recently, in-situ observations by Martin et al. [92] found that keyhole porosity during LB-PBF forms from bulges or instabilities within the vapor depression that become entrained within the solidifying material via Marangoni convection. Martin et al. [92] suggested that the circular shape of the keyhole pores was caused by pore spheroidization as they try to reduce their surface area. Bayat et al. [93] similarly suggested that the rounding of keyhole pores was a result of the hydrostatic pressure of the liquid metal that was acting on all sides of the pore.

Entrapped Gas Pores

Entrapped gas porosity relates to small (<20 µm), circular pores that can be found within as-built LB-PBF specimens [35] [86]. Their primary cause is the transfer of residual gas porosity from the powder feedstock to the as-built specimens. Gorden et al. [89] and Bobel et al. [94] observed this transfer in-situ, where entrapped gas pores from the powder would first transfer into the melt pool before becoming entrained during solidification. However, the relative transfer of these gas pores is quite low (<10%) as it seems that a significant number can escape prior to solidification [86] [89]. Besides this porosity transfer, the re-melting of other defects that contain entrapped gas (e.g. lack of fusion and keyhole porosity) [86] and the low packing density of the powder bed [95] have been identified as other potential sources of entrapped gas porosity.

2.5.3 Residual Stresses and Cracking

As discussed in Section 2.4, the rapid cooling rates of LB-PBF allow for the martensitic transformation to take place, creating an as-built material with a low ductility. This rapid cooling also results in the formation of internal residual stresses that, combined with the brittle martensite, can lead to cracking and delamination of the as-built component [5] [96] [97]. Processing parameters can be tailored to address this issue. While past studies have found that the magnitude of internal residual stresses decreases as the VED decreases [98] [99] [100], the most common mitigation strategy is the use of build

plate preheating, which lowers the magnitude of the internal residual stresses and helps prevent cracking defects in the as-built specimens [4] [5] [101].

Residual stresses are classified based upon the scale at which they operate [6]. Type I residual stresses are macro-stresses that relate to the component as a whole; Type II residual stresses are micro-stresses that relate to the stresses of individual grains; and Type III residual stresses are nano-stresses that relate to the stresses present at the atomic scale. In LB-PBF the focus has primarily been on Type I stresses as they can cause part distortion [6] and can negatively affect mechanical properties [102].

The formation of Type I residual stresses during LB-PBF can be described using two mechanisms. The first is the temperature gradient mechanism, which describes the formation of residual stresses within the solidified layers that are located directly underneath the layer being processed [103]. Due to the rapid heating of the uppermost surface and the relatively slow heat conduction through the layers below, a steep temperature gradient develops, causing the upper layer to expand and the lower layers to restrict this expansion. These changes lead to compressive strains within the material (Figure 16). Eventually, if these strains rise above the yield strength, plastic deformation occurs within the top layer. As this plastically deformed layer cools, the initial compressive strain is converted into residual tensile stress that can induce cracking (Figure 16). The second mechanism indicates that during solidification, the volume shrinkage that occurs within the melt pool will be restricted by the layers below it, again leading to the formation of residual tensile stress that can cause cracking within the component. Although these mechanisms provide a basic understanding of residual stresses, the reality during LB-PBF is much more complicated, as the non-uniform and highly localized solidification means that different sections will be heated and cooled differently, creating a non-uniform distribution of residual stresses within the as-built component [6].

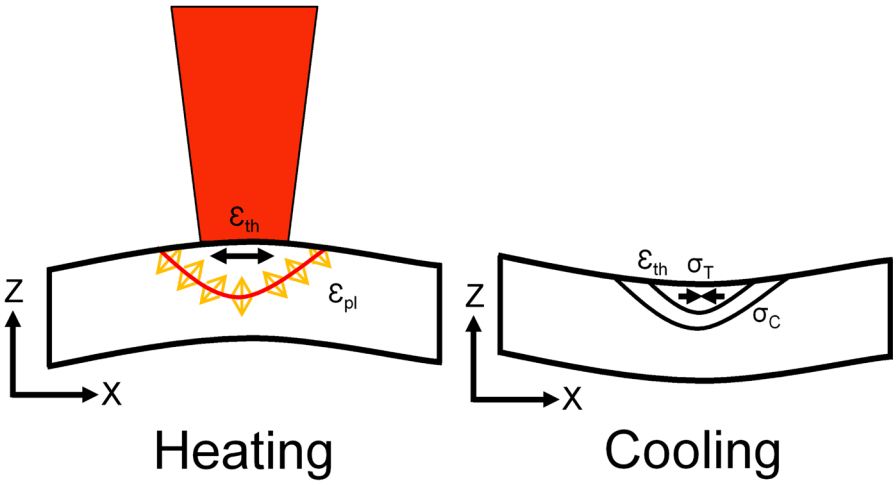

Figure 16: Schematic outlining the temperature gradient mechanism. Adapted from [103].

In addition, residual stresses form due to the martensitic transformation, as it causes a volume increase within the material [72] that induces compressive stresses at the specimen surface. These compressive residual stresses were found by both Yan et al. [7] and Mertens et al. [4] in LB-PBF-produced H13 tool steel. Mertens et al. [4] also examined the influence of build plate preheating and found that at low preheating temperatures (<200°C), a compressive stress was present at the specimen surface due to the martensitic transformation. However, as the preheating increased to temperatures above 300°C, the residual stresses changed from a compressive state to a tensile state. The cause was that at these preheating temperatures the martensitic transformation could be suppressed, allowing for thermally induced tensile stresses to form instead.

2.6 LB-PBF OF PLAIN CARBON AND LOW-ALLOY STEELS

This section provides an overview of the published research on the LB-PBF production of plain carbon and low-alloy steels.

2.6.1 Plain Carbon Steels

To date, a limited number of studies have examined the laser-based AM production of plain carbon steels. The most recent such study was conducted over 10 years ago, when the capabilities of laser-based AM could only sinter the material and not achieve full melting.

The first study on plain carbon steels was conducted by Murali et al. [104] and dealt with the laser sintering of a powder mixture of iron and graphite (0.78%) using an Nd:YAG pulsed laser source. The authors found that the laser was not powerful enough to fully melt the material, leading to a partially melted and sintered structure. This partially sintered structure led to noticeable porosity within the as-built specimens, with specimen densities of approximately 91%.

Simchi and Pohl [105] examined the role of graphite addition (0.4, 0.8, 1.2 and 1.6 wt.%) on the laser sintering of iron powder using a continuous CO_2 laser source. They found that the addition of graphite would increase the sintering kinetics, which was mainly attributed to the role of dissolved carbon. However, if intense energy inputs were applied, then large cracks would form within the specimens and cause delamination of the sintered layers. Using the highest-performing processing parameters, specimen densities of approximately 80% could be achieved.

Rombouts et al. [45] examined the selective laser melting of Fe and Fe-C powder mixtures using an Nd:YAG laser source. They found that the addition of carbon improved the surface quality of the produced components and caused the internal porosity to become less irregular and more spherically shaped. They attributed these differences to the improved wetting behavior when the carbon content was greater. Using the highest-performing parameters, specimen densities of ~93% could be achieved.

The most comprehensive research on the subject, conducted by Nakamoto et al. [106], dealt with the laser sintering of carbon steel powders (between 0.33 to 1.04 wt.% C) using a CO_2 laser source. They were able to achieve fully dense specimens (according to Archimedes measurements) and found that increasing the carbon content decreased the volume fraction of porosity and decreased the VED that was required to achieve fully dense specimens. Single- and double-track experiments also found that increasing the carbon content improved the wettability between the melt track and the substrate as well as the overlap between neighboring melt tracks. This improved wetting behavior was attributed to the lowered surface tension and melting temperature of the alloys with increased carbon content.

2.6.2 Low-Alloy Steels

Like plain carbon steels, limited studies have examined the LB-PBF production of low-alloy steels. However, studies on low-alloy steels have been conducted relatively recently (within the last five years) and have used modern AM equipment that can achieve full melting of the material during processing.

Cr-Mo Low-Alloy Steels

Wang and Kelly [107] examined the LB-PBF production of 4140 low-alloy steel using an EOS M280 machine equipped with an Yb-fiber laser and a build plate preheating of 80°C. Mechanical testing found the as-built specimens to have comparable properties to wrought 4140 alloys, with the as-built specimens displaying a slightly higher yield/tensile strength, a lower elongation and a comparable Charpy toughness. With respect to the as-built specimens, some directional anisotropy was observed as specimens oriented in the x-axis displayed a slightly higher yield strength, tensile strength, elongation and Charpy toughness in comparison to z-axis specimens.

Li et al. [46] focused on parameter development and mechanical property testing of a micro-lattice structure made from 4130 low-alloy steel that was produced using an SLM 280 HL machine equipped with an Yb-fiber laser. They found that both the tensile and energy absorption properties of the as-built 4130 material were high and attributed these values to the heterogeneously tempered martensitic microstructure that they found within their as-built material.

Lastly, Damon et al. [108] examined parameter optimization and mechanical property testing of a 4140 low-alloy steel using an SLM 290 machine equipped with an Yb-fiber laser and a build plate preheating of 200°C. After parameter optimization, they achieved specimen densities of up to 99.8%, although micro-cracks could still be found within these specimens. Subsequent mechanical testing found the LB-PBF specimens to have comparable properties to conventionally quenched and tempered and as-built plus quenched and tempered specimens. They attributed this finding to the intrinsic heat treatment that takes place during LB-PBF, giving the as-built material a tempered state. Additional testing found that the hardness of the as-built specimens was dependent upon the VED, where increasing the VED lowered the material hardness. The authors attributed this effect to a greater intrinsic heat treatment as the VED increased.

Ni-Cr-Mo Low-Alloy Steels

Jelis et al. [109], [110], [111] conducted studies on 4340 low-alloy steel utilizing an EOS M270 machine equipped with an Yb-fiber laser, in which the use of build plate preheating was not specified.

The first study [109] focused on parameter development and mechanical property testing of stress-relieved specimens that were produced using virgin and once-recycled powder. They found that the stress-relieved specimens displayed similar tensile properties to conventionally wrought material. Additionally, they found that the virgin and once-recycled powder specimens had similar tensile properties.

The second study [110] focused on mechanical property testing in the as-built, stress-relieved and heat-treated states. It also examined the influence of build orientation. Results indicated that in the as-built and stress-relieved states, the mechanical properties were inferior to those of a wrought material and below those of an as-built material that had been subsequently heat treated. Additionally, the as-built and stress-relieved specimens displayed some directional anisotropy, with specimens oriented in the x-axis displaying slightly improved mechanical properties in comparison to z-axis specimens.

The third study [111] examined the influence of layer thickness and internal powder porosity on the mechanical properties of heat-treated specimens. Results indicated that using a layer thickness of 40 µm (versus 20 µm) improved the build rate by up to 40% while maintaining similar mechanical properties. However, an increased layer thickness caused a reduction in the materials' ductility. In terms of powder porosity, it was found that if a substantial number of pores were present within the powder, then they would be transferred to the as-built specimens.

CHAPTER 3 – EXPERIMENTAL METHODS

3.1 MATERIALS

Plain Carbon Steels

Pre-alloyed, inert gas atomized powder, supplied by Höganäs AB, was used as the feedstock material for the analyzed plain carbon steels. Seven different plain carbon steel grades were examined across carbon contents of 0.03 to 1.1 wt.% C (Table 1), with each examined powder grade having a supplied sieve fraction of 20–63 µm.

Table 1: Chemical composition (wt.%) of the examined plain carbon steels as stated by the powder supplier.

	C	Si	Mn	S	O	N
Fe-0.03C	0.03	0.09	0.05	0.008	0.21	0.007
Fe-0.06C	0.06	0.10	0.06	0.008	0.12	0.006
Fe-0.12C	0.12	0.09	0.09	0.011	0.05	0.008
Fe-0.2C	0.20	0.10	0.09	0.007	0.04	0.007
Fe-0.45C	0.45	0.18	0.15	0.007	0.03	0.012
Fe-0.75C	0.75	0.18	0.08	0.007	0.07	0.013
Fe-1.1C	1.10	0.16	0.08	0.007	0.05	0.008

Low-Alloy Steels

Pre-alloyed, open furnace metallurgy and inert gas atomized powder, supplied by Sandvik Additive Manufacturing and Höganäs AB, was used as the feedstock material for the analyzed low-alloy steels. Five different low-alloy steel grades were examined (Table 2), with the analysis of the 4140 alloy involving two alloy compositions, a low-carbon and a high-carbon variant that were referred to as 4140LC and 4140HC, respectively. These powder grades had supplied sieve fractions of 15–45 µm (4140LC, 4340, 8620) and 20–53 µm (4130, 4140HC), respectively.

Table 2: Chemical composition (wt.%) of the examined low-alloy steels as stated by the powder suppliers.

	C	Ni	Cr	Mo	Mn	Si	P	S
4130	0.34	-	1.0	0.20	0.60	0.30	0.01	0.006
4140 HC	0.47	-	1.0	0.20	0.60	0.20	0.011	0.007
4140 LC	0.43	-	1.0	0.20	0.75	0.29	0.006	0.004
4340	0.43	1.9	1.0	0.30	0.60	0.17	0.010	0.005
8620	0.20	0.7	0.5	0.23	0.80	0.35	0.010	0.005

3.2 LB-PBF PROCESSING

Laser based powder bed fusion (LB-PBF) was conducted using an EOS M100 machine (EOS GmbH, Germany) equipped with an Yb-fiber laser. The laser had a maximum laser power of 200 W and a beam diameter of ~40 µm. During processing, the build plate was not preheated, and an oxygen content of ~0.1% was maintained within the building chamber using Ar gas. In terms of the scanning strategy, only core exposure was used when producing the plain carbon and low-alloy steel specimens. For the exposure, a 5-mm stripe scan pattern was used along with a scan rotation angle of 67°.

3.3 SPECIMEN PREPARATION

Metallography

Analysis of the plain carbon steels involved the production of 5 x 5 x 5 mm^3 specimens, while analysis of the low-alloy steels involved the production of 10 x 10 x 10 mm^3 specimens. After LB-PBF, these specimens were removed from the build plate and subsequently sectioned along the XZ plane using a Buehler ISOMET 2000 precision saw (Figure 17). They were subsequently mounted using a Struers Citopress machine then ground and polished down to 1 μm with diamond paste using a Struers TegraPol machine. After polishing, select specimens were etched using Nital etchant (3%).

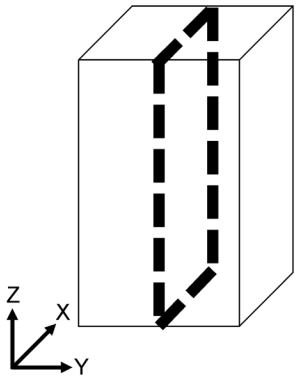

Figure 17: Schematic outlining where sectioning of the as-built specimens was conducted.

Fractography Specimens

Fractography analysis was conducted on select plain carbon and low-alloy steel specimens that displayed cracking defects. These specimens were prepared by making a 1–2 mm incision on the specimen surface in a direction that was parallel to a revealed crack on the opposite specimen surface. This incision was then used to facilitate fracturing of the specimen to reveal the crack, which was then analyzed using scanning electron microscopy (SEM).

Post-LB-PBF Heat Treatment

After LB-PBF, select low-alloy steels specimens underwent additional heat treatment using a Carbolite CWF 1200 box furnace that maintained an inert Ar atmosphere during heat treatment. The first heat treatment was a quenching procedure in which the specimens were first austenitized at 900°C for one hour, followed by quenching in oil. The second heat treatment involved the same quenching procedure followed by tempering at 500°C for two hours.

3.4 ANALYSIS TECHNIQUES

Optical Microscopy

A Zeiss Axiovision 7 light optical microscope (OM) was used to capture images of polished and etched specimen cross-sections. The microscope was equipped with an automated stage that allowed for image stitching when using the Zeiss Zencore 2.7 software.

Using OM images (with a resolution of at least 1.08 μm/pixel), two sets of image analyses were conducted. The first involved the measurement of the as-built specimen density using Image J software. This approach was chosen due to the relatively high accuracy of the technique in relation to computer tomography analysis [112]. Initially, the OM image of a specimen cross-section was loaded into the ImageJ software. Next, this image was cropped and converted into a binary image format to help

separate the pores from the specimen bulk (Figure 18). In this binary form, the area percentage of the pores could be measured. For each set of parameters, two to three specimens were analyzed.

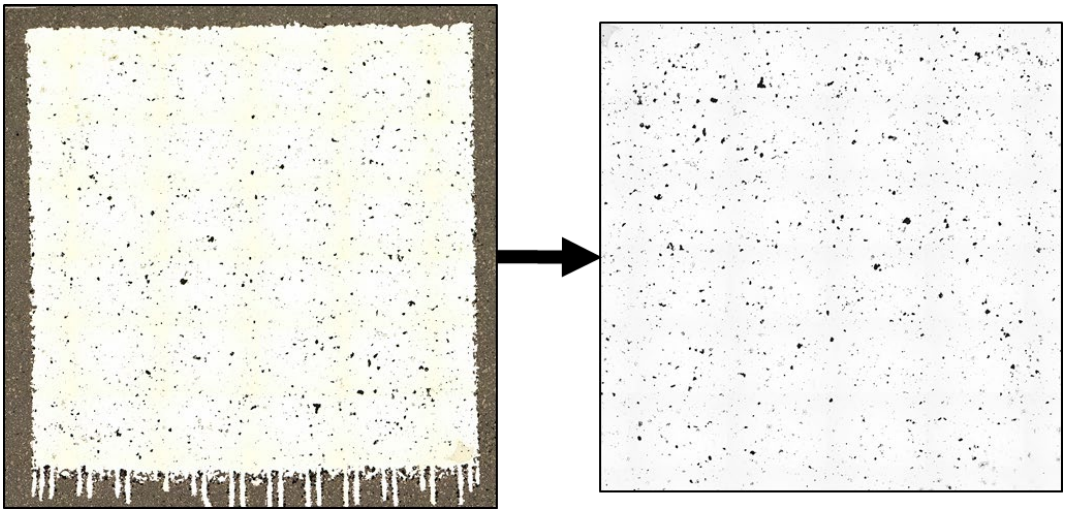

Figure 18: Initial optical microscopy image (left) of an 8620 alloy specimen that was subsequently cropped and converted into a binary image format (right) so it could be analyzed using the ImageJ software.

The second set of image analyses involved a quantitative characterization of individual pores within select plain carbon and low-alloy steel specimens. Using the same technique as before, the original image was cropped and converted into a binary format. Next, the shape characteristics of each pore were measured using the shape descriptor plug-in of the ImageJ software. During this analysis, non-porosity defects (e.g. cracks) were excluded, and any pore smaller than 20μm^2 was filtered out to reduce noise.

The analyzed shape descriptors included the roundness, aspect ratio and feret diameter. The feret diameter was used to define the size of each pore, as it represents the longest distance between any two points (Figure 19), while the aspect ratio and roundness were used to define the shape characteristics of each pore. The aspect ratio is a dimensionless shape factor that represents the ratio between the largest dimension (c) and the smallest dimension (a) that is perpendicular to c (Figure 19), where a value of 1 represents a perfect circle and any value above 1 represents a deviation to a more irregular shape. The roundness is also a dimensionless shape factor that describes how close a pore is to a perfect circle, with 0 representing a completely irregular shape and 1 representing a perfectly round circle. This shape factor is calculated using the pore area and the length of the major axis (c):

$$Roundness = \frac{4*Area}{\pi*c^2} \tag{3.1}$$

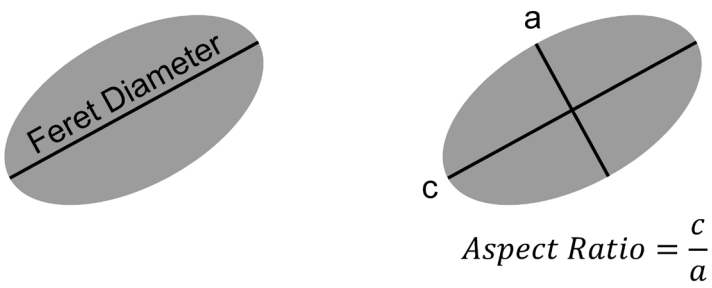

Figure 19: Schematic outlining the feret diameter and the aspect ratio.

Melt pool depth measurements were conducted on plain carbon and low-alloy steel specimens using the top layer of etched XZ specimen cross-sections (Figure 20). For each parameter set, 10 to 15 measurements of the melt pool depth were conducted.

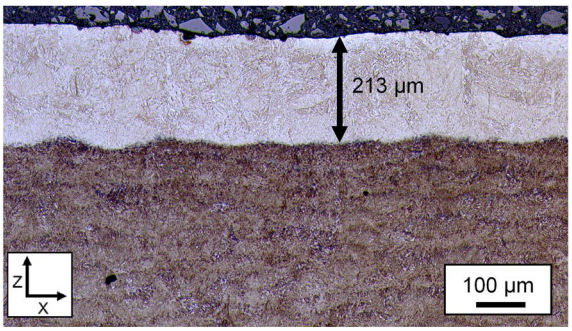

Figure 20: Melt pool depth measurement in a 4340 low-alloy steel specimen produced a 160 J/mm^3 using a 140 W laser power.

Scanning Electron Microscopy

SEM is a powerful characterization technique that produces high-magnification images and can reveal the microscopic information of a specimen such as the phase composition, topology, composition and crystallography, in addition to other physical and chemical properties [113]. The operating principle of SEM involves the creation of a focused beam of energized electrons via emission from a high-voltage electron source (up to 30 keV). After emission and subsequent beam refinement, the electron beam penetrates the specimen and interacts with specimen electrons down to a depth of 1 to 5 µm depending upon the specimen's atomic mass, the beam incidence angle and the accelerating voltage of the beam [114]. This interaction produces secondary electrons (SE), backscattered electrons (BSE), Auger electrons and characteristic X-rays (Figure 21).

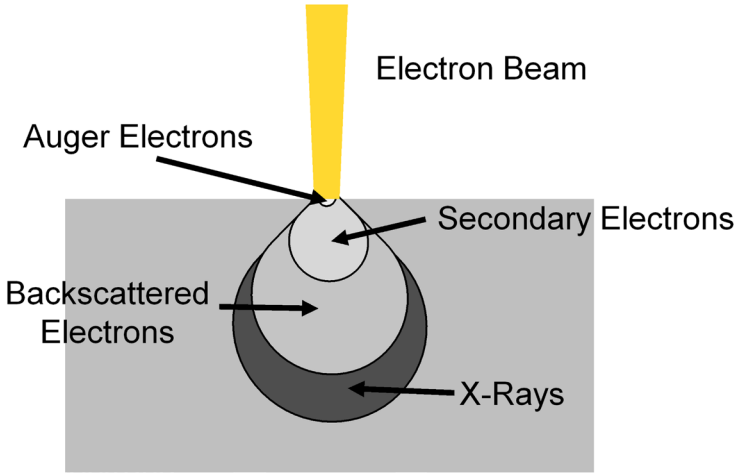

Figure 21: Schematic of the interaction volume during scanning electron microscopy. Adapted from [114].

SE are electrons that escape from the specimen at energies below 50 eV and are mainly knocked out of their atomic orbit by incoming incident electrons (Figure 22a). Since SE only escape from the near-surface regions, they provide topological information about the specimen. BSE, on the other hand, relate to higher-energy incident electrons that approach and interact with the atomic nucleus before being scattered and re-emerging out of the specimen (Figure 22b). Since the interaction depth of these electrons is greater, they do not provide the same topological contrast as SE. However, they can provide compositional contrast as the atomic mass of the element will influence the observed brightness of the

scattered electrons [114]. Besides SE and BSE, there is also the emission of Auger electrons and characteristic X-rays. Auger electrons are emitted from the atomic layers near the specimen surface, providing information on the surface chemistry, while characteristic X-rays are generated when an incident electron knocks out an inner-shell electron, causing an outer-shell electron to migrate and fill its place (Figure 22c). As this migration occurs, characteristic X-rays are emitted and can be used to obtain information regarding the chemical composition [114].

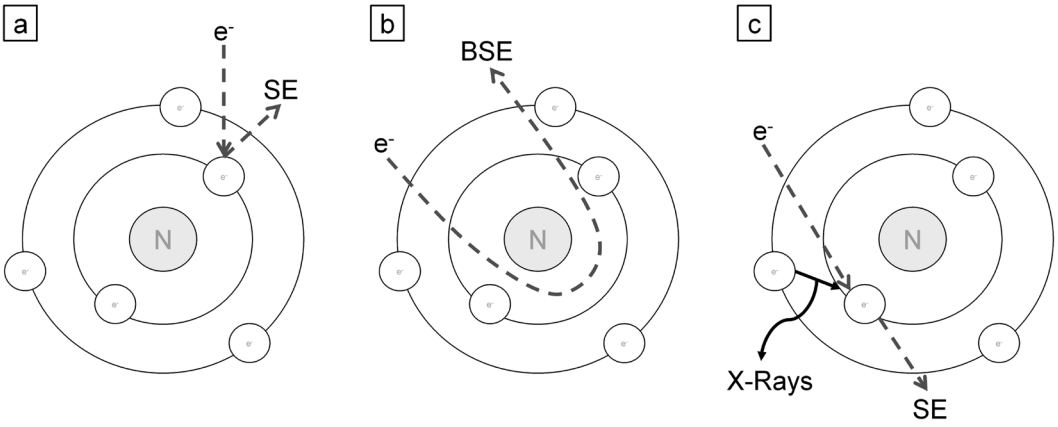

Figure 22: a) Schematic outlining the generation of secondary electrons (SE); b) schematic outlining the generation of backscattered electrons (BSE); c) schematic outlining the generation of characteristic X-rays when an electron from a higher-energy state fills the place of an ejected electron. Adapted from [114].

In this study, polished and etched specimen cross-sections were studied using a Leo Gemini 1550 high-resolution scanning electron microscope.

Electron Backscatter Diffraction

Electron backscatter diffraction (EBSD) is a SEM-based characterization technique that provides information regarding the morphology and crystallography of a material [115]. This is done by analyzing the diffraction patterns (captured by a fluorescent screen detector) when an electron beam contacts a slanted specimen. When this interaction occurs, the diffracted electrons create a group of large-angle cones that impinge upon the fluorescent screen, generating visible lines that are referred to as Kikuchi bands [115]. These lines are projections of the crystalline lattice geometry, providing information on the crystal structure and crystallographic orientation of a specimen that can be used to identify phases and crystallographic features.

In this study, EBSD analysis of select Fe-0.45C alloy specimens was conducted using a Nordlys II detector (Oxford Instruments) attached to a Leo Gemini 1550 SEM. During operation, an accelerating voltage of 20 kV was applied, at a working distance of 10 mm, with a step size of 0.25 μm. The collected EBSD data was subsequently analyzed using ARPGE 2.4 software [116] to reconstruct the parent austenite grains and to measure their size.

X-Ray Diffraction

X-ray diffraction (XRD) is an analysis technique that can be used to identify the crystallographic structure of a specimen. The working principle of XRD begins with the irradiation of X-rays onto a specimen while simultaneously varying the angle of incidence of the X-rays. These X-rays are then diffracted from the specimen and collected by detectors to measure the returned signal at specific incidence angles. With these values, the present phases can be identified by relating the diffraction angle to the inter-planar spacing using Bragg's law:

$$n\lambda = 2dsin\theta \tag{3.2}$$

Where n is the diffraction order, λ is the X-ray wavelength, d is the inter-planar spacing and θ is the angle at which the incident X-rays hit the specimen. Specific crystal structures have distinct signals at specified incidence angles, making it possible to identify a crystalline structure by comparing the measured signals to a known database. In this study, XRD analysis of select plain carbon steel specimens was carried out using a Bruker AXS D8 Advance diffractometer equipped with a Cr K_α source and operated at 35 kV using a beam current of 50 mA.

Chemical Analysis

Inert gas fusion was used to measure the oxygen content within select low-alloy steel specimens. To conduct this analysis, specimens were heated in a graphite or ceramic crucible to ~3000°C in an inert gas atmosphere. At this high temperature, the dissolved gases are driven off and, in the case of oxygen, will react to form carbon monoxide (CO) and carbon dioxide (CO_2). This CO and CO_2 is then quantified by infra-red detectors that measure the total released oxygen content [117]. A LECO ON836 elemental analyzer was used to conduct the inert gas fusion analysis.

Combustion analysis was used to measure the carbon content of the examined plain carbon and low-alloy steel powders. To conduct this analysis, specimens were combusted within an induction furnace that had a high flow of oxygen. The carbon present within the specimens reacted to form CO and CO_2, which was subsequently detected and measured using infrared absorption [118]. A LECO CS844 elemental analyzer was used to conduct the combustion analysis.

Simulation and Material Modeling

In this study, simulation and material modeling involved the use of two types of software. The first was ThermoCalc 2020b [119] with access to the TCFE10 database. This software utilizes a CALPHAD methodology for materials modeling, which is a phenomenological approach for the calculation of thermodynamic and kinetic properties of multi-component material systems [120]. Here, newly developed property model calculations were used to predict the martensite fraction and the martensite transformation temperatures. The calculation of the martensite fraction was based on an analytical equation derived by Huyan et al. [121], while the calculation of the martensite transformation temperatures was based on the modeling of the transformation barrier with fitted analytical equations [69]. The second software program was JMatPro v.11, which uses physically based material models to predict and calculate the properties of multi-component material systems [122].

3.5 MECHANICAL TESTING

Hardness

Vickers hardness (HV) testing was used to measure the macro- and micro-hardness of specimens across loads of 100 g to 10 kg. During this testing, a chosen load was applied to the specimen using a diamond indenter, creating a square-like indentation. Using the average diagonal of the indentation along with the applied force, the HV could be calculated, where F is the force (kgf) and d is the average diagonal (mm):

$$HV = \frac{1.8544*F}{d^2} \tag{3.3}$$

Measurement of the Vickers micro-hardness was conducted on plain carbon and low-alloy steel specimens using a DuraScan 70-G5 machine in accordance with the ASTM E384-17 standard [123].

CHAPTER 4 – SUMMARY OF RESULTS

This chapter summarizes the results of the appended papers. The first paper conducted an examination with Fe-0.03C powder to determine an acceptable set of laser based powder bed fusion (LB-PBF) parameters that were subsequently used to produce Fe-0.03C, Fe-0.45C and Fe-0.75C alloy specimens. The second paper investigated the LB-PBF fabrication of Fe-C alloys between 0.06 and 1.1 wt.% C, focusing on their as-built microstructure and processability. The third paper investigated the as-built microstructure and processability of low-alloy steels produced by LB-PBF, namely 4130, 4140, 4340 and 8620 alloys. In this summary, the results of the appended papers have been segmented into sections that focus on (i) the initial selection of the processing parameters, (ii) the as-built state of the microstructure and (iii) the LB-PBF processability of the examined alloys.

4.1 SELECTION OF ADEQUATE PROCESSING PARAMETERS

In **Paper I**, an initial investigation regarding the influence of hatch spacing and laser power was conducted on Fe-0.03C alloy specimens produced at layer thicknesses of 20 µm and 40 µm. The investigation determined that at a layer thickness of 20 µm, a hatch spacing of 70 µm and a laser power of 110 W was an adequate set of parameters to achieve high-specimen densities (>99%). When using a layer thickness of 40 µm, a hatch spacing of 40 µm and a laser power of 170 W was an adequate set of parameters to achieve high-specimen densities (>99%). Using each parameter set, Fe-0.03C specimens were produced at volumetric energy densities (VED) between 60 and 200 J/mm^3. This investigation found that the 20-µm specimens outperformed the 40-µm specimens at each tested VED. The inferior performance of the 40-µm specimens was caused by the presence of large, irregular pores (Figure 23). Since these pores occurred in all specimens (even those produced at high VED), their formation was attributed to process instabilities that were likely connected to issues of powder spreading and powder bed packing density when using a larger layer thickness.

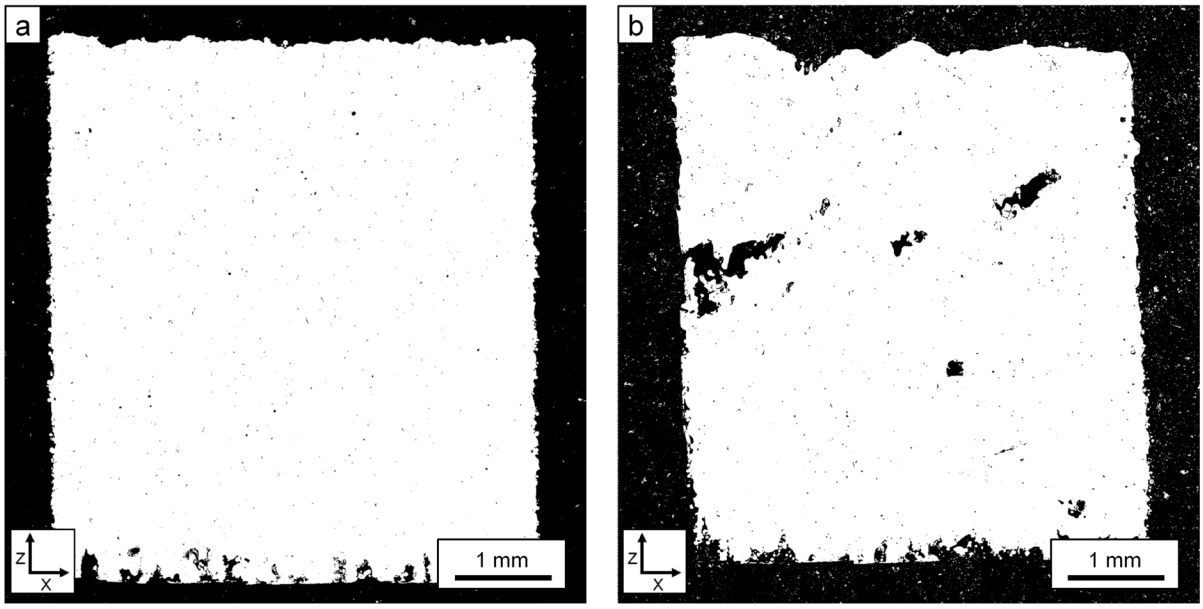

Figure 23: a) Fe-0.03C alloy produced at 130 J/mm^3 using a 20-µm layer thickness; b) Fe-0.03 alloy produced at 130 J/mm^3 using a 40-µm layer thickness showing large, irregular pores.

4.2 AS-BUILT MICROSTRUCTURE

In **Paper II** and **Paper III**, the as-built microstructure of the plain carbon and low-alloy steel specimens was found to consist of tempered martensite that displayed an overlapping boundary structure (Figure

24a). These boundaries related to the heat-affected regions of deposited melt tracks and were preferentially revealed after Nital (3%) etching, becoming more prominent as the carbon content of the alloy increased. Additional scanning electron microscopy (SEM) analysis in **Paper II** revealed that alloys with ≥0.75 wt.% C contained retained austenite within these boundary regions (Figure 24b), where the fraction of retained austenite increased as the carbon content increased. This retention of austenite was due to the depression of the martensite transformation temperatures at these elevated levels of carbon content.

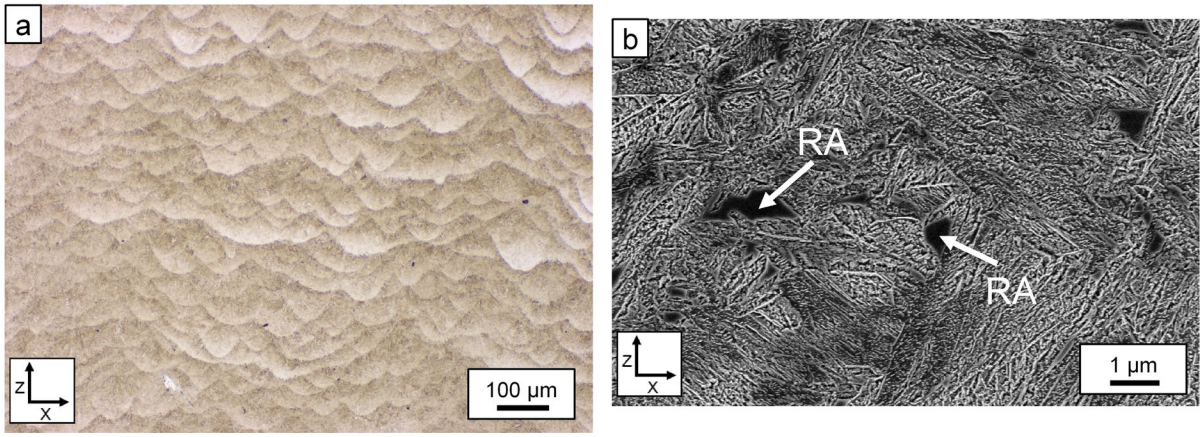

Figure 24: a) Heat-affected boundary structures in an Fe-0.75C alloy specimen produced at 150 J/mm^3. b) Retained austenite located within the heat-affected boundary structure of an Fe-0.75C alloy specimen produced at 200 J/mm^3. Results from **Paper II**.

In **Paper II** and **Paper III,** the tempered state of the martensite was correlated by both SEM and hardness testing. SEM analysis revealed the presence of nano-scale precipitates (<100 nm) within the martensite (Figure 25), which are likely cementite or transitional carbides that form during the intrinsic heat treatment of LB-PBF. Hardness testing, meanwhile, found the as-built specimens to have a similar hardness to quenched and tempered specimens, supporting the hypothesis that tempering of the martensite occurs in-situ during LB-PBF.

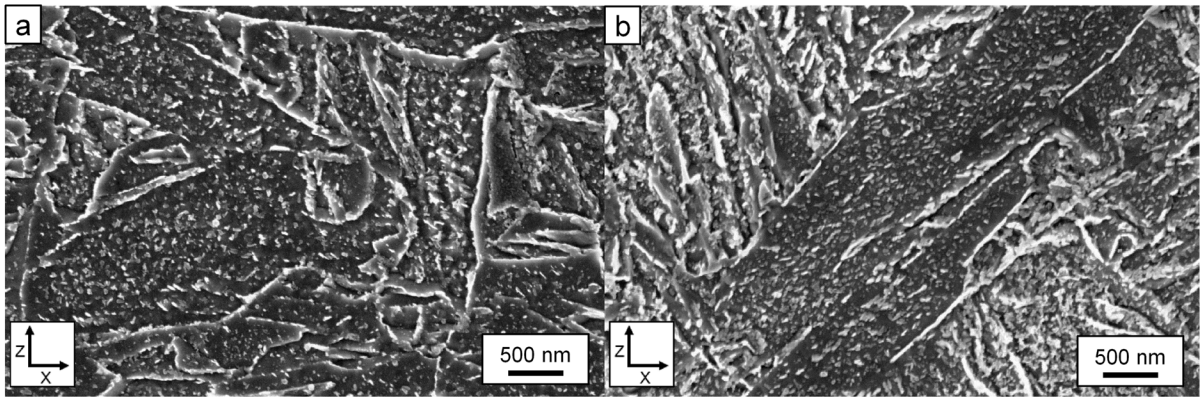

Figure 25: SEM images of nano-scale precipitates found in: a) Fe-0.2C alloy specimen produced at 130 J/mm^3; b) 4140LC alloy specimen produced at 60 J/mm^3 using a 110 W laser power.

Results in **Paper III** also revealed that most tempering within the as-built specimens occurred during the deposition of a new layer onto a previously solidified layer, as micro-hardness testing indicated that the regions directly below a new layer had already transitioned into a tempered state (Figure 26).

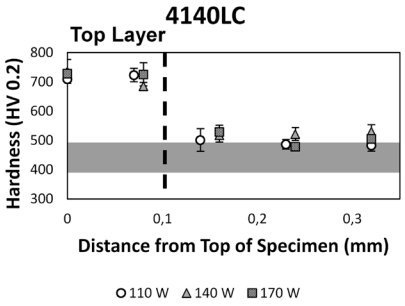

Figure 26: Micro-hardness along the z-direction in a 4140LC alloy specimen produced at 110 J/mm^3. Average as-built hardness of specimen bulk is depicted as the grey region. Results from **Paper III.**

4.3 Processability by Laser Based Powder Bed Fusion

4.3.1 Porosity Defects in As-Built Specimens

Results in **Paper I, Paper II** and **Paper III** indicated that the specimen density was dependent on the chosen VED and that their relationship could be segmented into three regions (Figure 27a). At low VED (Region I), specimens contained large, irregular pores (Figure 27b). As these pores formed at low VED and contained un-melted/partially sintered particles, they could be identified as lack of fusion porosity. Conversely, at high VED (Region III), specimens contained rounded, medium-sized pores (Figure 27d). As these pores formed at high VED and were located at the bottom of melt pool boundaries, they could be identified as keyhole porosity. In between these VED regions, high-density (>99.8%) specimens could be produced (Region II; Figure 27c). Results in **Paper III** also determined that the VED range of Region II increased as the laser power increased.

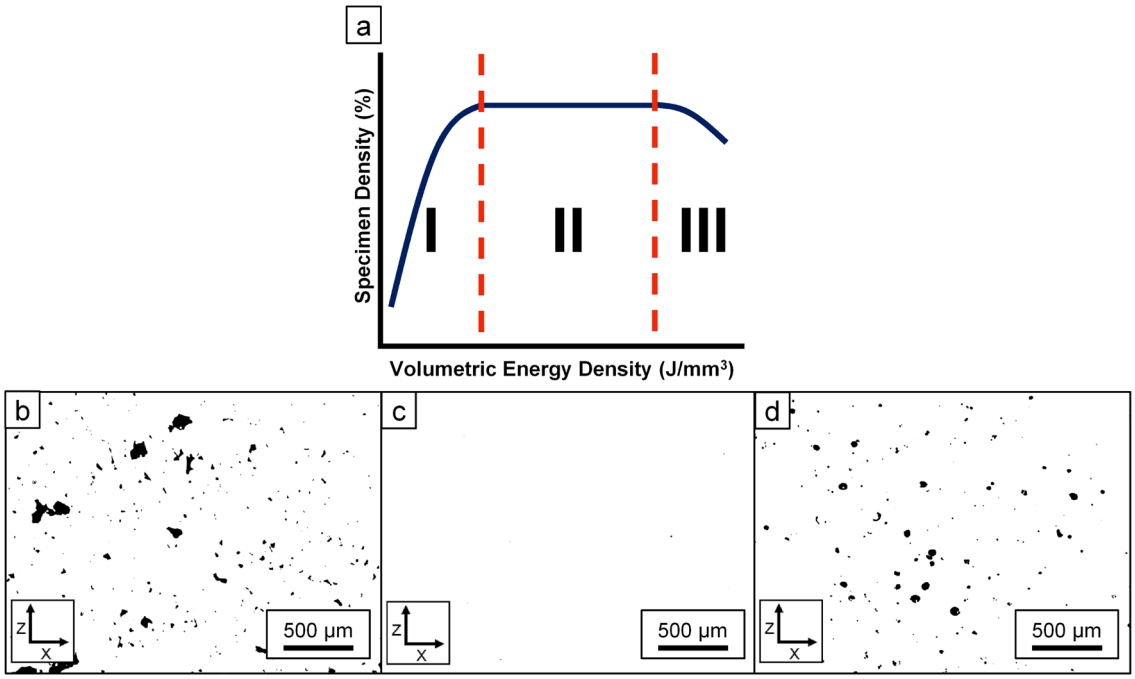

Figure 27: a) Schematic outlining the trend between the specimen density and the VED. b) Characteristic specimen from Region I with lack of fusion porosity (4340 alloy produced at 60 J/mm^3 using a 140 W laser power). b) Characteristic specimen from Region II with minimal porosity (4340 alloy produced at 110 J/mm^3 using a 140 W laser power). c) Characteristic specimen from Region III with keyhole porosity (4340 alloy produced at 185 J/mm^3 using a 110 W laser power).

Paper III also involved a detailed image analysis of the present porosity within the three regions. It was found that the porosity in Region I was the most numerous, largest and most irregular in terms of its shape (Table 3 and Figure 28), which corresponded to the visual observations of lack of fusion porosity. Region II specimens contained the fewest number of pores that were relatively small (<20 µm) and circular in shape, while Region III specimens contained circular pores that were more numerous and larger than the porosity in Region II specimens, but smaller than the porosity in Region I specimens. These characteristics pointed to the presence of keyhole porosity as well as the enhanced presence of small (<20 µm), circular pores.

Table 3: Average pore characteristics in 4140HC alloy specimens. Results from **Paper III**.

	Number of Pores	Average Aspect Ratio	Average Roundness	Porosity Area Faction (%)
Region I (4140HC)	5000	2.0 ± 0.9	0.58 ± 0.2	4.6
Region II (4140HC)	1000	1.6 ± 1.2	0.72 ± 0.2	0.1
Region III (4140HC)	2900	1.5 ± 0.5	0.69 ± 0.2	1.4

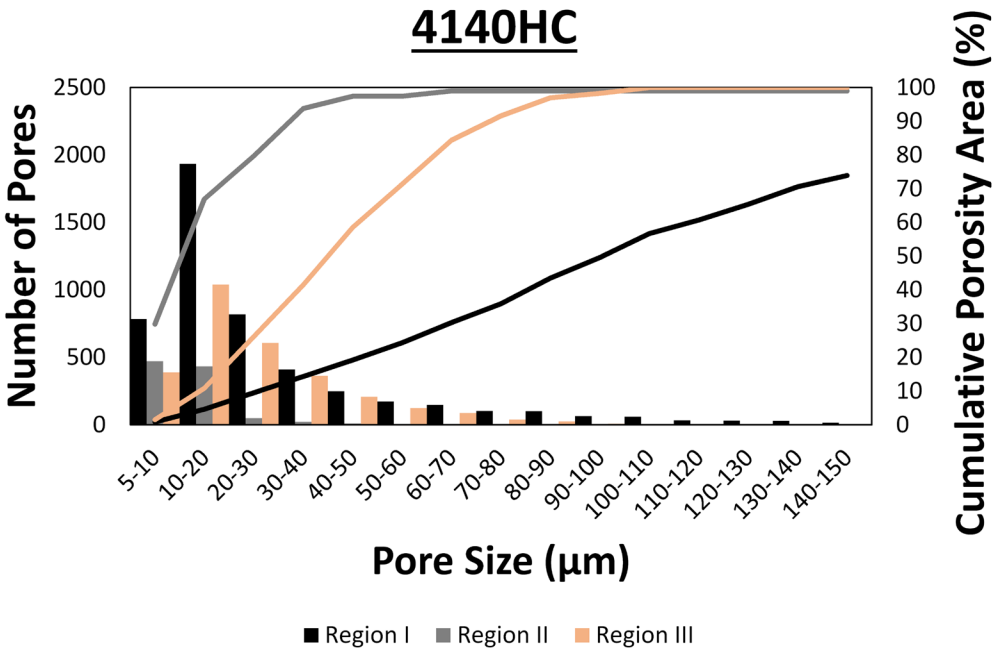

Figure 28: Histogram and cumulative porosity area in 4140HC alloy specimens from each process region. Results from **Paper III**.

Paper II showed that in addition to the VED, the specimen density was dependent on the carbon content of the alloy, with two major impacts identified. The first was that at low VED, the specimen density improved as the carbon content increased, as increasing the carbon content limited the formation of lack of fusion porosity (Figure 29). The second was that at high VED, the specimen density deteriorated as the carbon content increased, as increasing the carbon content promoted the formation of keyhole porosity (Figure 29). The reduction in lack of fusion porosity at lower VED was due to the influence of carbon on the wettability and flowability of the melt pool, as increased carbon contents lower the surface tension and the viscosity, improving the infiltration behavior. Concerning the increase in keyhole porosity, it was observed that the melt pool depth increased as the carbon content increased, pointing to a greater likelihood for keyhole porosity to form.

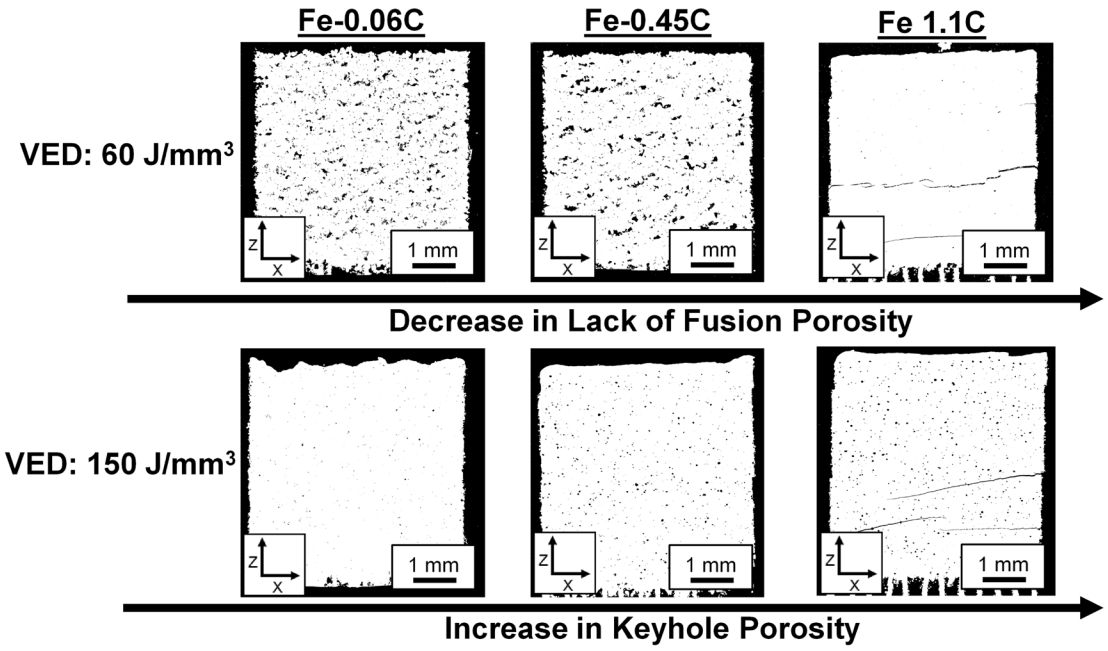

Figure 29: Cross-sections of Fe-C alloy specimens produced at 60 J/mm^3 revealed a decrease in lack of fusion porosity with higher carbon content, while cross-sections of Fe-C alloy specimens produced at 150 J/mm^3 revealed an increase in keyhole porosity with higher carbon content. Results from **Paper II**.

4.3.2 Cracking Defects in As-Built Specimens

In **Paper I**, **Paper II** and **Paper III**, cracking was observed in all Fe-0.75C and Fe-1.1C alloy specimens and in select 4140LC, 4140HC, 4340 and Fe-0.45C alloy specimens. These cracks originated at the specimen surface and grew towards the specimen center (Figure 30a). In **Paper II** and **Paper III**, observation of the microstructure as well as micro-hardness measurements across the crack interface revealed similar characteristics in both regions, pointing to a cold cracking phenomenon. This was confirmed via SEM analysis of fractography specimens (Figure 30b), which found that transgranular cleavage was the dominant micro-failure mechanism.

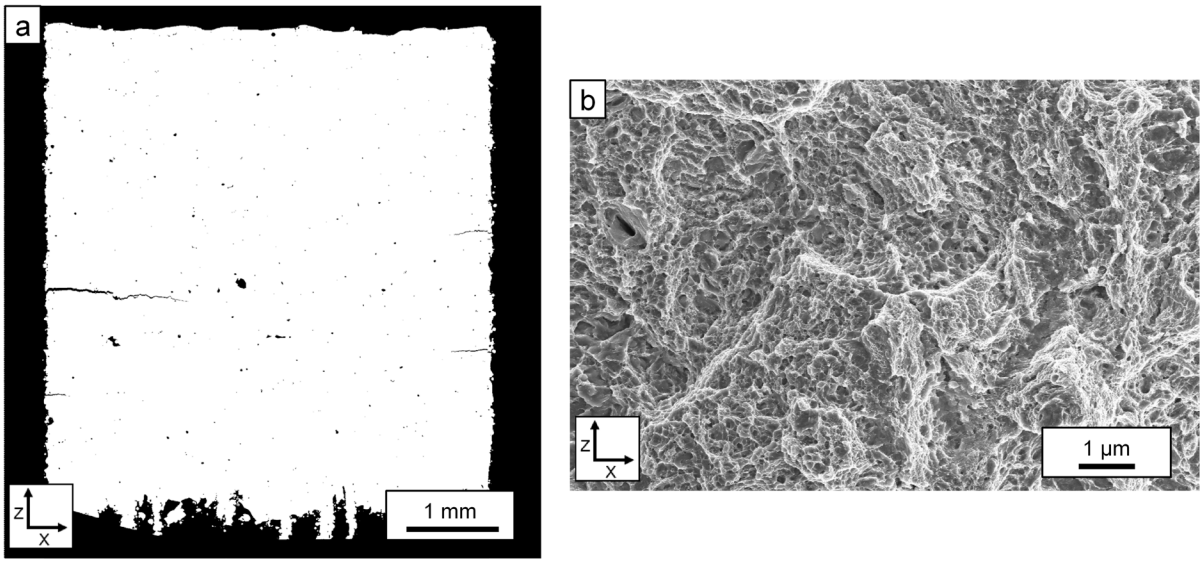

Figure 30: a) Cracking in an Fe-0.75C alloy specimen produced at 130 J/mm^3. b) SEM image of the crack fractography in an Fe-0.75C alloy specimen produced at 160 J/mm^3 at 5-kx magnification.

In **Paper II** and **Paper III**, cracking in the 4140LC, 4140HC, 4340 and Fe-0.45C alloy specimens only occurred below certain VEDs. For the Fe-0.45C alloy, cracking occurred in specimens produced below 90 J/mm^3, while cracking in the 4140LC, 4140HC and 4340 alloy specimens was dependent upon the laser power (Table 4), where increasing the laser power reduced the VED that prevented cold cracking.

Table 4: Maximum VED at which cold cracking occurred for the listed low-alloy steels. Results from **Paper III**.

	110W	**140W**	**170W**
4140LC	110 J/mm^3	100 J/mm^3	80 J/mm^3
4140HC	110 J/mm^3	110 J/mm^3	110 J/mm^3
4340	110 J/mm^3	110 J/mm^3	80 J/mm^3

This susceptibility to cracking at lower VED and laser power is due to the higher hardness of the as-built specimens produced at these conditions (Figure 31 and Figure 32), which, in turn, is the result of a less intensive intrinsic heat treatment during LB-PBF. **Paper II** and **Paper III** found that the melt pool depth was linearly proportional to both the VED and the laser power (Figure 31 and Figure 32). This meant that as these parameters increased, the volume of material that was melted and subsequently re-heated also increased, enhancing the in-situ tempering and ultimately reducing the specimen hardness until said specimen could accommodate its internal residual stresses without cracking. From these results, specific hardness thresholds could be established that defined whether cold cracking would occur: ≥425 HV for Fe-C alloys, >460 HV for 4140 alloys and >500 HV for 4340 alloys.

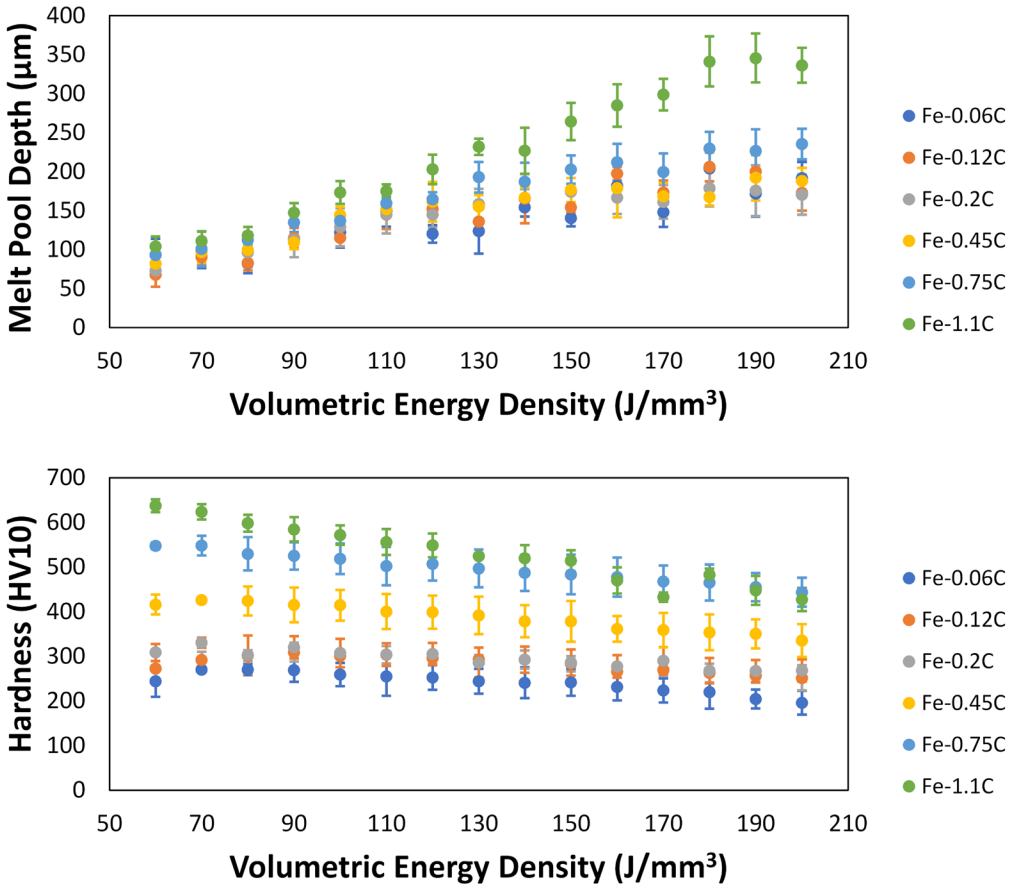

Figure 31: Melt pool depth and hardness as a function of the VED for the investigated Fe-C alloys. Results from **Paper II**.

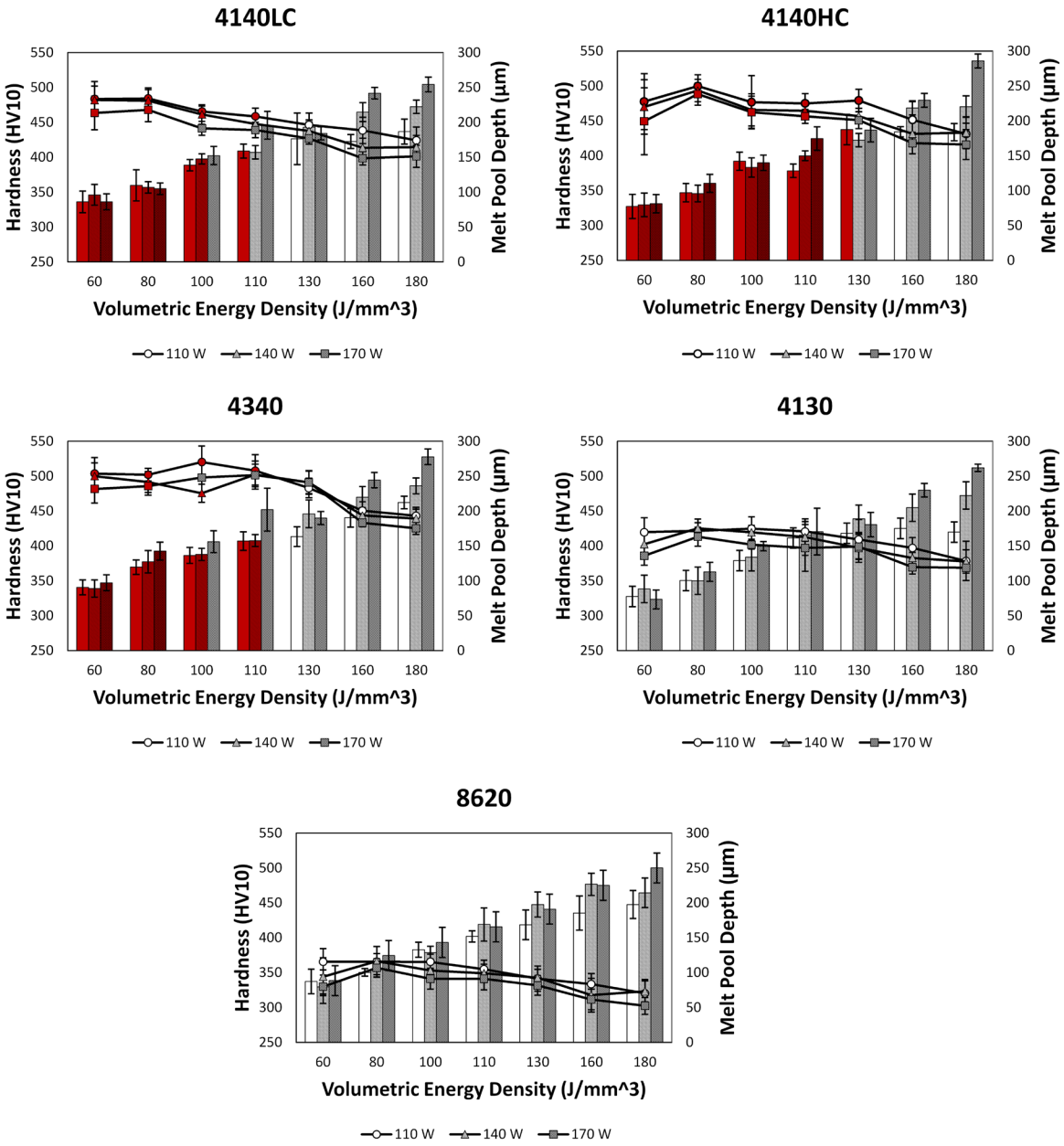

Figure 32:Variation in specimen hardness and melt pool depth as a function of the VED for the 4130, 4140HC, 4140LC, 4340 and 8620 alloys. Hardness is displayed as a scatter chart, while the melt pool depth is displayed as a bar chart. The VEDs at which cold cracking occurred are indicated with red fill. Results from **Paper III**.

In addition to the VED and laser power, the as-built specimen hardness was dependent on the carbon content, with increased levels of carbon increasing the specimen hardness (Figure 31 and Figure 32). This explains why alloys with lower carbon contents (4130, 8620 and all Fe-C alloys <0.45 wt.% C) did not display cracking regardless of the chosen processing parameters and also why alloys with high levels of carbon (Fe-0.75C and Fe-1.1C) were unable to avoid cracking.

4.3.3 Processing Windows for High-Density, Defect-Free Specimens

From the results of **Paper II**, a processing window for the Fe-C system could be established that produced high-density (>99.8%), defect-free specimens without the requirement of build plate preheating (Figure 33). If one assumed the use of build plate preheating, it would further expand the

processability window, improve the process robustness and decrease the cracking susceptibility of the as-built specimens.

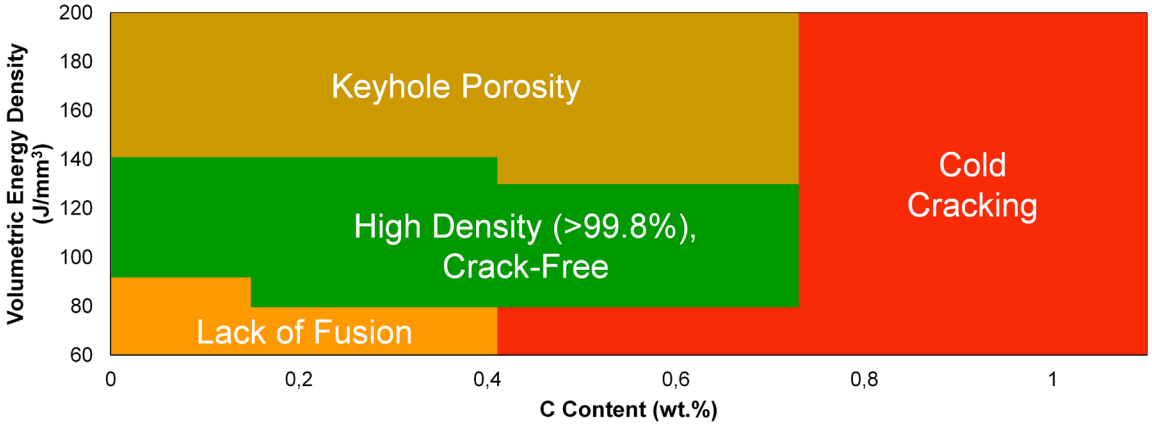

Figure 33: Processing window for the Fe-C system as a function of the VED and the carbon content. Results from **Paper II**.

From the results of **Paper III**, processing windows were established for each low-alloy steel that produced high-density (>99.8%), defect-free specimens without the requirement of build plate preheating (Table 5).

Table 5: Processing windows that produced high-density (>99.8%), defect-free specimens for each low-alloy steel at laser powers of 110 W, 140 W and 170 W. Results from **Paper III**.

	110W	**140W**	**170W**
4130	100–140 J/mm^3	110–180 J/mm^3	110–180 J/mm^3
4140 LC	110–185 J/mm^3	110–180 J/mm^3	110–200 J/mm^3
4140 HC	130–160 J/mm^3	110–160 J/mm^3	110–180 J/mm^3
4340	110–130 J/mm^3	110–130 J/mm^3	100–180 J/mm^3
8620	110–130 J/mm^3	100–160 J/mm^3	100–200 J/mm^3

CHAPTER 5 – CONCLUSIONS

From the results of this licentiate thesis study, the following conclusions can be made:

The as-built microstructure of the plain carbon and low-alloy steel specimens was primarily composed of tempered martensite that resulted from the intrinsic heat treatment of laser based powder bed fusion (LB-PBF). In alloys with ≥0.75 wt.% C, retained austenite was observed in the heat-affected boundary regions of the as-built microstructure, forming due to the depression of the martensite transformation temperatures at these elevated levels of carbon.

Porosity within the as-built specimens was dependent on the chosen volumetric energy density (VED) and could be categorized using three regions. At low VED (Region I), specimens contained large, irregular pores that related to lack of fusion porosity, while at high VED (Region III), specimens contained rounded, medium-sized pores that related to keyhole porosity. At VED ranges between these two (Region II), high-density (>99.8%) specimens could be produced, with the range of Region II increasing as the laser power was increased. Porosity within the as-built specimens was also dependent on the carbon content of the alloy, where increasing the carbon content limited the formation of lack of fusion porosity at low VED while increasing the formation of keyhole porosity at high VED. These effects were due to the increase in melt wettability and flowability and the increased melt pool depth at higher carbon contents, respectively.

Cracking was observed in some plain carbon and low-alloy steel specimens and was the result of a cold cracking phenomenon. Its occurrence was dependent on the hardness of the as-built material, and hardness thresholds could define whether cold cracking would occur: ≥425 HV for Fe-C alloys, >460 HV for 4140 alloys and >500 HV for 4340 alloys. Due to this hardness dependence, the VED, laser power and carbon content were important factors that influenced crack susceptibility. Increasing the VED or laser power, reduced the hardness of the material as these factors enhanced the intrinsic heat treatment that took place during LB-PBF. This means that for some alloys, if the VED or laser power were large enough, cold cracking can be avoided. The carbon content directly influenced the specimen hardness, helping explain why plain carbon (<0.45 wt.% C) and low-alloy steel (4130 and 8620) specimens with low carbon contents did not display cracking defects, as well as why plain carbon steels with high carbon contents (≥0.75 wt.% C) could not avoid cracking even when using the largest VED and laser power.

From these findings, robust processing windows were established for the plain carbon and low-alloy steels that could produce high-density (>99.8%), defect-free specimens without the requirement of build plate preheating. For the plain carbon steels, these processing windows were based on the VED and the carbon content, while the processing windows for the low-alloy steels were based on the VED and the laser power.

CHAPTER 6 – FUTURE WORK

From the results of this licentiate thesis study, the following is recommended for future research:

A deeper investigation regarding the influence of the intrinsic heat treatment on the produced microstructure is recommended. Specifically, future research might examine the transition between the newly deposited layer and the re-heated regions directly below this layer, as results in Paper III indicated that most material tempering occurred between these two regions.

Results in Paper II revealed the noticeable loss of oxygen between the powder feedstock and the as-built specimens, where the oxygen loss was somewhat dependent on the carbon content of the alloy. As such, it would be of interest to conduct a more thorough investigation into how the carbon content and the processing conditions influence the loss of alloying elements during LB-PBF.

Lastly, it would be of interest to translate the developed processing parameters of the low-alloy steels to a larger machine that is more commonly used in serial production (e.g. EOS M290). Work with the larger LB-PBF machine should also examine the influence of build plate preheating and be used to produce mechanical property specimens with the necessary statistics. Further work on the tailoring of the heat treatment for these alloys should also be performed to maximize the mechanical properties, and to provide a comparison to specimens that have been conventionally produced and heat treated.

ACKNOWLEDGEMENTS

First, I would like to thank my supervisor Prof. Eduard Hryha and my co-supervisor Prof. Lars Nyborg for giving me the opportunity to take part in this exciting research and for their invaluable guidance and support during this time.

I would also like to recognize the Centre for Additive Manufacturing – Metal (CAM^2), that is supported by Vinnova, for providing the funding and framework under which this project has taken place. Special thanks go out to Dr. Peter Harlin (Sandvik Additive Manufacturing) and Adj. Prof. Sven Bengtsson (Höganäs AB) for their collaboration in terms of planning, testing and for providing the powder feedstock that was used in this research.

I would like to thank and recognize my former master's thesis students Robert Steinlechner and Rasmus Gunnerek for their fantastic work, interesting discussions and camaraderie during our time together.

Furthermore, I would like to acknowledge the research engineers Dr. Yiming Yao, Roger Sagdahl, and Håkan Millqvist for their help regarding the practical work that was done in this research.

Thanks also goes out to my past and present colleagues at the Department of Industrial and Materials Science, whose presence has always made my day more enjoyable and who are always there to provide support whenever it is needed.

Special thanks go out to my family, whether it is those back in Canada or those in Sweden and Finland for their support during this time.

Finally, I would like to thank my loving wife Ida Hearn for her incredible love and support, without which I would not have been able to make it to this point. Also, I want to thank the little one who is still in mom's tummy for giving me all the inspiration I could ever ask for.

REFERENCES

[1] D. Bourell, W. Frazier, H. Kuhn and M. Seifi, ASM Handbook®, Volume 24 - Additive Manufacturing Processes, ASM International, 2020.

[2] "Wohlers Report 2018," Wohlers Associates, Detriot, 2018.

[3] J. Davis, ASM Specialty Handbook Carbon and Alloy Steels, ASM International, 1996.

[4] R. Mertens, B. Vrancken, N. Holmstock, Y. Kinds, J.-P. Kruth and J. Van Humbeeck, "Influence of powder bed preheating on microstructure and mechanical properties of H13 tool steel SLM parts," *Physics Procedia,* no. 83, pp. 882-890, 2016.

[5] K. Kempen, B. Vrancken, S. Buls, L. Thijs, J. Van Humbeeck and J. Kruth, "Selective Laser Melting of Crack-Free High Density M2 High Speed Steel Parts by Baseplate Preheating," *Journal of Manufacturing Science and Engineering,* vol. 136, 2014.

[6] J. Bartlett and X. Li, "An overview of residual stresses in metal powder bed fusion," *Additive Manufacturing,* vol. 27, pp. 131-149, 2019.

[7] J. Yan, D. Zheng, H. Li, X. Jia, J. Sun, Y. Li, M. Qian and M. Yan, "Selective laser melting of H13: microstructure and residual stress," *Journal of Materials Science,* vol. 52, pp. 12476-12485, 2017.

[8] L. Malefane, W. du Preez, M. Maringa and A. du Plessis, "Tensile and high cycle fatigue properties of annealed Ti6Al4V (ELI) specimens produced by direct metal laser sintering," *South African Journal of Industrial Engineering,* vol. 29, pp. 299-311, 2018.

[9] O. Andreau, E. Pessard, I. Koutiri, J.-D. Penot, C. Dupuy, N. Saintier and P. Peyre, "A competition between the contour and hatching zones on the high cycle fatigue behaviour of a 316L stainless steel: Analyzed using X-ray computed tomography," *Materials Science and Engineering A,* vol. 757, pp. 146-159, 2019.

[10] H. Carlton, A. Haboub, G. Gallegos, D. Parkinson and A. MacDowell, "Damage evolution and failure mechanisms in additively manufactured stainless steel," *Materials Science & Engineering A,* vol. 651, pp. 406-414, 2016.

[11] N. Larrosa, W. Wang, N. Read, M. Loretto, C. Evans, J. Carr, U. Tradowsky, M. Attallah and P. Withers, "Linking microstructure and processing defects to mechanical properties of selectively laser melted AlSi10Mg alloy," *Theoretical and Applied Fracture Mechanics,* vol. 98, pp. 123-133, 2018.

[12] H. Krell, A. Rottger, K. Geenen and W. Theisen, "General investigations on processing tool steel X40CrMoV5-1 with selective laser melting," *Journal of Materials Processing Technology,* vol. 255, pp. 679-688, 2018.

[13] R. Dörfet, J. Zhang, B. Clausen, H. Freisse, J. Schumacher and F. Vollersten, "Comparison of the fatigue strength between additively and conventionally fabricated tool steel 1.2344," *Additive Manfuacturing,* no. 27, pp. 217-223, 2019.

[14] G. Krauss, Physical Metallurgy and Heat Treatment of Steel, American Society for Metals, 1985.

[15] J. Dossett and G. Totten, ASM Handbook, Volume 04D - Heat Treating of Irons and Steels., ASM International, 2014.

[16] A. I. H. Committee, ASM Handbook, Volume 01 - Properties and Selection: Irons, Steels, and High-Performance Alloys., ASM International, 1990.

[17] P. Harvey, Engineering Properties of Steels, American Society for Metals, 1982.

[18] "Standard Terminology for Additive Manufacturing - General Principles - Terminology," ASTM International, West Conshohocken, PA, 2015.

[19] C. Zhang, F. Chen, Z. Huang, J. Mingyong, G. Chen, Y. Ye, Y. Lin, W. Liu, B. Chen, Q. Shen, L. Zhang and E. Lavernia, "Additive manufacturing of functionally graded materials: A review," *Materials Science & Engineering A,* vol. 764, 2019.

[20] Introduction to Additive Manufacturing Technology: 3rd Edition, European Powder Metallurgy Association, 2019.

[21] A. Strondl, O. Lyckfeldt, H. Brodin and U. Ackelid, "Characterization and Control of Powder Properties for Additive Manufacturing," *JOM,* no. 67, pp. 549-555, 2015.

[22] J. Benson and E. Snyders, "The need for powder charcterization in the additive manufacturing industry and the establishment of a national facility," *The South African Journal of Industrial Engineering,* no. 26, pp. 104-114, 2015.

[23] D. Schulze, Powder and bulk solids: behavior, characterization, storage and flow, Berlin: Springer, 2008.

[24] P. Karapatis, "A sub-process approach of selective laser sintering," EPFL, Lausanne, 2002.

[25] D. Riabov, E. Hryha, M. Rashidi, S. Bengstsson and L. Nyborg, "Effect of atomization on surface oxide composition in 316L stainless steel powders for additive manufacturing," *Surface and Interface Analysis,* vol. 52, no. 11, pp. 694-706, 2020.

[26] H. Gruber, C. Luchian, E. Hryha and L. Nyborg, "Effect of Powder Recycling on Defect Formation in Electron Beam Melted Alloy 718," *Metallurgical and Materials Transactions A,* vol. 51, no. 5, pp. 2430-2433, 2020.

[27] S. Vock, B. Klöden, A. Kirchner, T. Weissgärber and B. Kieback, "Powders for powder bed fusion: a review," *Progress in Additive Manufacturing,* no. 4, pp. 383-397, 2019.

[28] J. Weinberg, Design and Implementation of an Experimental and Numerical Framework for Powder Recoating Research in Selective Laser Melting, Massachusetts Institute of Technology, 2018.

[29] C. Qui, C. Panwisawas, M. Ward, H. Basoalto, J. Brooks and M. Attallah, "On the role of melt flow into the surface structure and porosity development during selective laser melting," *Acta Materialia,* no. 96, pp. 72-79, 2015.

[30] R. Gunnerek, "Improving Build Rate of Low Alloy Steels Produced by Laser Powder Bed Fusion: Influence of layer thickness on processability," Chalmers University of Technology, 2020.

[31] C. Pauzon, P. Foret, E. Hryha, T. Arunprasad and L. Nyborg, "Argon-helium mixtures as Laser-Powder Bed Fusion atmospheres: Towards increased build rate of Ti-6Al-4V," *Journal of Materials Processing Technology,* no. 279, 2020.

[32] C. Pauzon, "The Process Atmosphere as a Parameter in the Laser-Powder Bed Fusion Process," Chalmers University of Technology, Gothenburg, 2019.

[33] C. Pauzon, A. Leicht, U. Klement, P. Foret and E. Hryha, "Effect if the Process Gas and Scan Speed on the Properties and Productivity of Thin 316L Structures Produced by Laser-Powder Bed Fusion," *Metallurgical and Materials Transactions A,* no. 51, pp. 5339-5350, 2020.

[34] H. Ali, H. Ghadbeigi and K. Mumtaz, "Effect of scanning strategies on residual stress and mechanical properties of Selective Laser Melted Ti6Al4V," *Materials Science & Engineering A,* no. 712, pp. 175-187, 2018.

[35] T. DebRoy, H. Wei, J. Zuback, T. Mukherjee, J. Elmer, J. Milewski, A. Beese, A. Wilson-Heid, A. De and W. Zhang, "Additive manufacturing of metallic components - Process, structure and properties," *Progress in Materials Science,* vol. 92, pp. 112-224, 2018.

[36] W. Meiners, K. Wissenbach and A. Gasser, "Shaped Body Especially Prototype or Replacement Part Production". DE Patent DE19649865C1, 1996.

[37] H. Lee, C. Lim, M. Low, N. M. V. Tham and Y.-J. Kim, "Lasers in Additive Manufacturing: A Review," *International Journal of Precision Engineering and Manufacturing-Green Technology,* no. 4, pp. 307-322, 2017.

[38] Y. Li and D. Gu, "Parametric Analysis of thermal behavior during selective laser melting additive manufacturing of aluminum alloy powder," *Materials and Design,* vol. 63, pp. 856-867, 2014.

[39] W. Di, Y. Yongqiang, S. Xubin and C. Yonghua, "Study on energy input and its influences on single-track, multi-track, and multi-layer SLM," *The International Journal of Advanced Manufacturing Technology,* vol. 58, pp. 1189-1199, 2012.

[40] R. Cunningham, C. Zhao, N. Parah, C. Kantzos, J. Pauza, K. Fezzaa, T. Sun and A. Rollett, "Keyhole threshold and morpohology in laser melting revealed by ultrahigh-speed x-ray imaging," *Science,* vol. 363, pp. 849-852, 2019.

[41] Z. Francis, "The Effects of Laser and Electron Beam Spot Size in Additive Manufacturing Processes," Carnegie Mellon University, Pittsburgh, 2017.

[42] J. Metelkova, Y. Kinds, K. Kempen, C. de Formanoir, A. Witvrouw and B. Van Hooreweder, "On the influence of laser defocusing in Selective Laser Melting of 316L," *Additive Manufacturing,* no. 23, pp. 161-169, 2018.

[43] A. Gusarov, S. Grigoriev, M. Volosova, Y. Melnik, A. Laskin, D. Kotoban and A. Okunkova, "On productivity of laser additive manufacturing," *Journal of Materials Processing Technology,* vol. 261, pp. 213-232, 2018.

[44] V. Matilainen, H. Piili, A. Salminen and O. Nyrhila, "Preliminary investigation of keyhole phenomena during single layer fabrication in laser additive manufacturing of stainless steel," *Physics Procedia,* vol. 78, pp. 377-387, 2015.

[45] M. Rombouts, J. Kruth, L. Froyen and P. Mercelis, "Fundamentals of Seletive Laser Melting of alloyed steel powders," *CIRP Annals,* vol. 55, no. 1, pp. 187-192, 2006.

[46] X. Li, Y. Tan, H. Willly, P. Wang, W. Lu, M. Cagirici, C. Ong, T. Herng, J. Wei and J. Ding, "Heterogenously tempered martensitic high strength steel by selective laser melting and its micro-lattice: Processing, microstructure, superior performance and mechanisms," *Materials and Design,* vol. 178, 2019.

[47] M. Tang, P. Pistorius and J. Beuth, "Prediction of lack-of-fusion porosity for powder bed fusion," *Additive Manufacturing,* vol. 14, pp. 39-48, 2017.

[48] T. Mukherjee and T. DebRoy, "Mitigation of lack of fusion defects in powder bed fusion additive manufacturing," *Journal of Manufacturing Processes,* vol. 36, pp. 442-449, 2018.

[49] I. Koutiri, E. Pessard, P. Peyre, O. Amlou and T. De Terris, "Influence of SLM process parameters on the surface finish, porosity rate and fatigue behavior of as-built Inconel 625 parts," *Journal of Materials Processing Technology,* no. 255, pp. 536-546, 2018.

[50] A. Martin, N. Calta, S. Khairallah, J. Wang, P. Depond, A. Fong, V. Thampy, G. Guss, A. Kiss, K. Stone, C. Tassone, J. Weker, M. Toney, T. van Buuren, Matthews and M, "Dynamics of pore formation during laser powder bed fusion additive manufacturing," *Nature Communications,* vol. 10, 2019.

[51] J. Pakkanen, "Designing for Additive Manufacturing -Product and Process Driven Design for Metals and Polymers," Politecnico di Torino, Torino, 2018.

[52] X. Wang, T. Laoui, J. Kruth, B. Lauwers and L. Froyen, "Direct Selective Laser Sintering of Hard Metal Powders: Experimental Study and Simulation," *The International Journal of Advanced Manufacturing Technology,* no. 19, pp. 351-357, 2002.

[53] A. Simchi, "Direct laser sintering of metal powders: Mechanism, kinetics and microstructural features," *Materials Science and Engineering A,* no. 428, pp. 148-158, 2006.

[54] M. Matthews, G. Guss, S. Khairallah, A. Rubenchik, P. Depond and W. King, "Denudation of metal powder layers in laser powder bed fusion," *Acta Materialia,* no. 114, pp. 33-42, 2016.

[55] S. Katayama, "Introduction: fundamentals of laser welding," in *Handbook of Laser Welding Technologies*, Woodhead Publishing, 2013, pp. 3-16.

[56] C. Panwisawas, B. Perumal, R. Ward, N. Turner, R. Turner, J. Brooks and H. Basoalto, "Keyhole formation and thermal fluid flow-induced porosity during laser fusion welding in titanium alloys: Experimental and modelling," *Acta Materialia,* vol. 126, pp. 251-263, 2017.

[57] S. Ly, A. Rubenchik, S. Khairallah, G. Guss and M. Matthews, "Metal vapor micro-jet controls material redistribution in laser powder bed fusion additive manufacturing," *Scientific Reports,* no. 7, 2017.

[58] U. Bertoli, G. Guss, S. Wu, M. Matthews and J. Schoenung, "In-situ characterization of laser-powder interaction and cooling rates through high-speed imaging of powder bed fusion additive manufacturing," *Materials and Design,* no. 135, pp. 385-396, 2017.

[59] X. He, J. Norris, P. Fuerschbach and T. DebRoy, "Liquid metal expulsion during laser spot welding of 304 stainless steel," *Journal of Physics D: Applied Physics,* vol. 39, no. 3, 2006.

[60] B. Keene, "Review of data for the surface tension of iron and its binary alloys," *International Materials Review,* vol. 33, no. 1, pp. 1-36, 1988.

[61] K. Mills, B. Keene, R. Brooks and A. Shirali, "Maragoni Effects in Welding," *Philosophical Transactions: Mathematical, Physical and Engineering Sciences,* vol. 356, no. 1739, pp. 911-925, 1998.

[62] S. Kou, Welding Metallurgy: Second Edition, Hoboken, New Jersey: John Wiley & Sons, Inc., 2003.

[63] Y. Li and D. Gu, "Parametric analysis of thermal behavior during selective laser melting additive manufacturing of aluminum alloy powder," *Materials and Design,* no. 63, pp. 856-867, 2014.

[64] A. Leicht, M. Rashidi, U. Klement and E. Hryha, "Effect of process parameters on the microstructure, tensile strength and productivity of 316L parts produced by laser powder bed fusion," *Materials Characterization,* vol. 159, 2020.

[65] P. Bajaj, A. Hariharan, A. Kini, P. Kurnsteiner, D. Raabe and E. Jägle, "Steels in additive manufacturing: A review of their microstructure and properties," *Materials Science & Engineering A,* vol. 772, 2020.

[66] G. Krauss, Steels - Processing, Structure, and Performance (2nd Edition), ASM International, 2015.

[67] A. Marder and G. Krauss, "The Morphology of Martensite in Iron-Carbon Alloys," *Trans. ASM,* vol. 60, pp. 651-660, 1967.

[68] C. Roberts, "Effect of Carbon on the Volume Fractions and Lattice Parameters of Retained Austenite and Martensite," *Trans. AIME,* vol. 197, pp. 203-204, 1953.

[69] A. Hanumantharaju, "Thermodynamic modelling of martensite start temperature in commercail steels," KTH Royal Institute of Technology, Stockholm, 2017.

[70] H. Yang and H. Bhadeshia, "Austenite grain size and the martensite-start temperature," *Scripta materialia,* vol. 60, pp. 493-495, 2009.

[71] S. van Bohemen and L. Morsdorf, "Predicting the Ms temperature of steels with a thermodynamic based model including the effect of the prior austenite grain size," *Acta Materialia,* vol. 125, pp. 401-415, 2017.

[72] E. Pereloma and D. Edmonds, Phase Transformations in Steels: Diffusionless Transformations, High Strength Steels, Modelling and Advanced Analytical Techniques, Elsevier Science & Technology, 2012.

[73] P. Krakhmalev, I. Yadroitsava, G. Fredriksson and I. Yadroitsev, "In situ heat treatment in selective laser melted martensitic AISI 420 stainless steels," *Materials and Design,* vol. 87, pp. 380-385, 2015.

[74] P. Kurnsteiner, M. Wilms, A. Weisheit, P. Barriobero-Vila, E. Jägle and D. Raabe, "Massive nanoprecipitation in an Fe-19Ni-xAl maraging steel triggered by the intrinsic heat treatment during laser metal deposition," *Acta Materiala,* vol. 129, pp. 52-60, 2017.

[75] P. Kurnsteiner, M. Wilms, A. Weisheit, B. Gault, E. Jägle and D. Raabe, "High-strength Damascus steel by additive manufacturing," *Nature,* vol. 582, pp. 515-519, 2020.

[76] M. Rombouts, "Selective Laser Sintering/Melting of Iron-Based Powders," University of Leuven, 2006.

[77] J. Kruth, L. Froyen, J. Van Varenbergh, P. Mercelis, M. Rombouts and B. Lauwers, "Selective laser melting of iron-based powder," *Journal of Materials Processing Technology,* vol. 149, pp. 616-622, 2004.

[78] R. Li, J. Liu, Y. Shi, L. Wang and W. Jiang, "Balling behavior of stainless steel and nickel powder during selective laser melting process," *The International Journal of Advanced Manufacturing Technology,* vol. 59, pp. 1025-1035, 2012.

[79] D. Gu and Y. Shen, "Balling phenomena in direct laser sintering of stainless steel powder: Metallurgical mechanisms and control methods," *Materials and Design,* vol. 30, pp. 2903-2910, 2009.

[80] H. Niu and I. Chang, "Instability of scan tracks of selective laser sintering of high speed steel powder," *Scripta Materialia,* vol. 41, no. 11, pp. 1229-1234, 1999.

[81] S. Das, "Physical Aspects of Process Control in Selective Laser Sintering of Metals," *Advanced Engineering Materials,* vol. 5, no. 10, 2003.

[82] Q. Guo, C. Zhao, L. Escano, Z. Young, L. Xiong, K. Fezzaa, W. Everhart, B. Brown, T. Sun and L. Chen, "Transient dynamics of powder spattering in laser powder bed fusion additive manufacturing process revealed by in-situ high-speed high-energy x-ray imaging," *Acta Materialia,* vol. 151, pp. 169-180, 2018.

[83] H. Gong, K. Rafi, H. Gu, G. Janaki Ram, T. Starr and B. Stucker, "Influence of defects on mechanical properites of Ti-6Al-4V components produced by selective laser melting and electron beam melting," *Materials and Design,* vol. 86, pp. 545-554, 2015.

[84] J. Stef, A. Poulon-Quintin, A. Redjaimia, J. Ghanbaja, O. Ferry, M. De Sousa and M. Goune, "Mechanism of porosity formation and influence on mechanical properties in selective laser melting of Ti-6Al-4V parts," *Materials and Design,* vol. 156, pp. 480-493, 2018.

[85] Q. Liu, J. Elambasseril, S. Sun, M. Leary, M. Brandt and P. Sharp, "The Effect of Manufacturing Defects on The Fatigue Behaviiour of Ti-6Al-4V Specimens Fabricated Using Selective Laser Melting," *Advanced Materials Research,* Vols. 891-892, pp. 1519-1524, 2014.

[86] R. Cunningham, S. Narra, C. Montgomery, J. Beuth and A. Rollett, "Synchrotron-Based X-ray Microtomography Characterization of the Effect of Processing Variables on Porosity Formation in Laser Powder-Bed Additive Manufacturing of Tu-6Al-4V," *JOM,* vol. 69, pp. 479-484, 2017.

[87] L. Thijs, F. Verhaeghe, T. Craeghs, J. Van Humbeeck and J.-P. Kruth, "A study of the microstructural evolution during selective laser melting of Ti-6Al-4V," *Acta Materialia,* vol. 58, pp. 3303-3312, 2010.

[88] W. King, W. Barth, V. Castillo, G. Gallegos, J. Gibbs, D. Hahn and C. R. A. Kamath, "Observation of keyhole-mode laser melting in laser powder-bed fusion additive manufacturing," *Journal of Materials Processing Technology,* vol. 214, pp. 2915-2925, 2014.

[89] J. Gordon, S. Narra, R. Cunningham, H. Liu, H. Chen, R. Suter, J. Beuth and A. Rollett, "Defect structure process maps for laser powder bed fusion additive manufacturing," *Additive Manufacturing,* vol. 36, 2020.

[90] R. Cunningham, "Defect Formation Mechanisms in Powder Bed Metal Additive Manufacturing," Carnegie Mellon University, 2018.

[91] J. Zhao, M. Easton, M. Qian, M. Leary and M. Brandt, "Effect of building direction on porosity and fatigue life of selective laser mleted AlSi12Mg alloy," *Materials Science & Engineering A,* vol. 729, pp. 76-85, 2018.

[92] A. Martin, N. Calta, J. Hammons, S. Khairallah, M. Nielsen, R. Shuttlesworth, N. Sinclair, M. Matthews, J. Jeffries, T. Willey and J. Lee, "Ultrafast dynamics of laser-metal interactions in additive manufacturing alloys captured by in situ X-ray imaging," *Materials Today Advances,* vol. 1, 2019.

[93] M. Bayat, A. Thanki, S. Mohanty, A. Wiyvrouw, S. Yang, J. Thorborg, N. Tiedje and J. Hattel, "Keyhole-induced porosities in Laser-based Powder Bed Fusion (L-PBF) of Ti6Al4V: High-fidelity modelling and experimental validation," *Additive Manufacturing,* vol. 30, 2019.

[94] A. Bobel, H. Jr., L, I. Chelladurai, A. Sachdev, T. Brown, W. Poling, R. Kubic, B. Gould, C. Zhao, N. Parab, A. Greco and T. Sun, "In situ synchrotron X-ray imaging of 4140 steel laser powder bed fusion," *Materialia,* vol. 6, 2019.

[95] B. Zhang, Y. Li and Q. Bai, "Defect Formation Mechanisms in Selective Laser Melting: A Review," *Chinese Journal of Mechanical Engineering,* vol. 30, pp. 515-527, 2017.

[96] Y. He, M. Zhong, J. Beuth and B. Webler, "A study of microstructure and cracking behavior of H13 tool steel produced by laser powder bed fusion using single-tracks, multi-track pads, and 3D cubes," *Journal of Materials Processing Technology,* vol. 286, 2020.

[97] E. Fonseca, A. Gabriel, L. Araujo, P. Santos, K. Campo and E. Lopes, "Assesment of laser power and scan speed influence on microstructural features and condolidation of AISI H13 tool streel processed by additive manufacturing," *Additive Manufacturing,* vol. 34, 2020.

[98] T. Mukherjee, V. D. A. Manvatkar and T. DebRoy, "Mitigation of thermal distortion during additive manufacturing," *Scripta Materialia,* vol. 127, pp. 79-83, 2017.

[99] Y. Liu, Y. Yang and D. Wang, "A study on the residual stress during seletive laser melting (SLM) of metallic powder," *The International Journal of Advanced Manufacturing Technology,* vol. 87, pp. 647-656, 2016.

[100] T. Simson, A. Emmel, A. Dwars and J. Böhm, "Residual stress measurements on AISI 316L samples manufactured by selective laser melting," *Additive Manufacturing,* vol. 17, pp. 183-189, 2017.

[101] M. Narvan, K. Al-Rubaie and M. Elbestawi, "Process-Structure-Property Relationships of AISI H13 Tool Steel Processed with Selective Laser Melting," *Materials,* vol. 12, 2019.

[102] P. Withers, "Residual stress and its role in failure," *Reports on Progress in Physics,* vol. 70, 2007.

[103] P. Mercelis and J. Kruth, "Residual stresses in selective laser sintering and selective laser melting," *Rapid Prototyping Journal,* pp. 254-265, 2006.

[104] K. Muralia, A. Chatterjee, P. Saha, R. Palai, S. Kumar, S. Roy, P. Mishra and A. Choudhury, "Direct selective laser sintering of iron-graphite powder mixture," *Journal of Materials Processing Technology,* vol. 136, pp. 179-185, 2003.

[105] A. Simchi and H. Pohl, "Direct laser sintering of iron-graphite powder mixture," *Materials Science and Engineering A,* vol. 383, pp. 191-200, 2004.

[106] T. Nakamoto, N. Shirakawa, Y. Miyata and H. Inui, "Selective laser sinering of high carbon steel powders studied as a function of carbon content," *Journal of Materials Processing Technology,* vol. 209, pp. 5653-5660, 2009.

[107] W. Wang and S. Kelly, "A Metallurgical Evaluation of the Powder-Bed Laser Additive Manufactured 4140 Steel Material," *JOM,* vol. 68, pp. 869-875, 2016.

[108] J. Damon, R. Koch, D. Kaiser, G. Graf, S. Dietrich and V. Shulze, "Process development and impact of intrinsic heat treatment on the mechanical performance of selective laser melted AISI 4140," *Additive Manufacturing,* vol. 28, pp. 275-284, 2019.

[109] E. Jelis, M. Clemente, S. Kerwien, N. Ravindra and R. Hespos, "Metallurgical and Mechanical Evaluation of 4340 Steel Produced by Direct Metal Laser Sintering," *JOM,* vol. 67, no. 3, pp. 582-589, 2015.

[110] E. Jelis, M. Hespos and N. Ravindra, "Process Evaluation of AISI 4340 Steel Manufactured by Laser Powder Bed Fusion," *JMEPEG,* vol. 27, pp. 63-71, 2018.

[111] E. Jelis, M. Hespos, S. Groeschler and R. Carpenter, "L-PBF of 4340 Low Alloy Steel: Influence of Feedstock Powder, Layer Thickness, and Machine Maintenance," *JMEPEG,* vol. 28, pp. 693-700, 2019.

[112] G. Kasperovich and J. Hausmann, "Improvement of fatigue resistance and ductility of TiAl6V4 processed by selective laser melting," *Journal of Materials Processing Technology,* no. 220, pp. 202-214, 2015.

[113] J. Goldstein, D. Newbury, J. Michael, N. Ritchie, J. Scott and D. Joy, Scanning Electron Microscopy and X-Ray Microanalysis - Fourth Edition, Springer, 2018.

[114] K. Vernon-Parry, "Scanning electron microscopy: an introduction," *III-Vs Review,* vol. 13, no. 4, pp. 40-44, 2000.

[115] A. Schwartz, M. Kumar, B. Adams and D. Field, Electron Backscatter Diffraction in Materials Science - Second Edition, Springer, 2009.

[116] C. Cayron, "ARPGE: a computer program to automatically reconstruct the parent grains from electron backscatter diffraction data," *Journal of Applied Crystallography,* vol. 40, pp. 1183-1188, 2007.

[117] J. Davis, Metals Handbook, Desk Edition (2nd Edition) - Bulk Elemental Analysis, ASM International, 1998.

[118] "Carbon & Sulfur Determination in Steel Plants and Foundries," Eltra GmbH, 2020. [Online]. Available: https://www.eltra.com/products/carbon-sulfur-determination/.

[119] J. Andersson, T. Helander, L. Höglund, P. Shi and B. Sundman, "Thermo-Calc and DICTRA, Computational tools for materials science," *Calphad,* vol. 26, pp. 273-312, 2002.

[120] "CALPHAD Methodology," Thermo-Calc Software, 2020. [Online]. Available: https://thermocalc.com/about-us/methodology/the-calphad-methodology/. [Accessed 29 12 2020].

[121] F. Huyan, P. Hedström, L. Höglund and A. Borgenstam, "A Thermodynamic-Based Model to Predict the Fraction of Martensite in Steels," *Metallurgical and Materials Transactions A,* vol. 47, pp. 4404-4410, 2016.

[122] "JMatPro: Pratical Software for Materials Properties," Senate Software UK, 2020. [Online]. Available: https://www.sentesoftware.co.uk/. [Accessed 29 12 2020].

[123] A. E384-17, Standard Test Method for Microindentation Hardness of MAterials, West Conshohocken, PA: ASTM International, 2017.